

Shan Sun · Rainer Bleck

# Multi-century simulations with the coupled GISS–HYCOM climate model: control experiments

Received: 22 April 2005 / Accepted: 4 November 2005 / Published online: 16 December 2005  
© Springer-Verlag 2005

**Abstract** Multi-century climate simulations obtained with the GISS atmospheric general circulation model coupled to the hybrid-isopycnic ocean model HYCOM are described. Greenhouse gas concentrations are held fixed in these experiments to investigate the coupled model's ability to reproduce the major features of today's climate with minimal drift. Emphasis is placed on the realism of the oceanic general circulation and its effect on air–sea exchange processes. Several model runs using different closures for turbulent vertical exchange as well as improvements to reduce vertical numerical diffusion are compared with climate observations. As in previous studies, the Southern Ocean emerges as the Achilles Heel of the ocean model; deficiencies in its physical representation had far-reaching consequences in early experiments with the coupled model and have provided the strongest impetus for model improvement. The overarching goal of this work is to add diversity to the pool of ocean models available for climate prediction and thereby reduce biases that may stand in the way of assessing climate prediction uncertainty.

---

## 1 Introduction

The coupled general circulation model (CGCM) has emerged as a versatile tool for exploring causes and effects of mechanisms that give rise to variability in the

earth's climate system. One important goal for today's CGCMs is to reach a skill level where they can reproduce the prominent features of the current climate without artificial corrections to fluxes across the air–sea interface. This goal is within reach: recent improvement of model physics and model numerics are now allowing a number of CGCMs to settle on a relatively stable and realistic mean state and to run over longer periods without resorting to flux adjustment.

However, local defects in model solutions can still be quite large. The simulated convective depth in the Southern Ocean, for example, is often too large compared to observations, leading to unrealistic surface temperatures and salinities—as well as sea ice loss—as slightly warmer, saltier water is brought up from the deeper ocean at an excessive rate. The problem arises in many non-eddy resolving ocean models and is believed to be related to (1) errors in the parameterization of eddy-induced advection, which is more important in the Southern Ocean than elsewhere due to the absence of meridional boundary currents; (2) the simplicity of the convective adjustment scheme; and (3) the lack of much needed vertical resolution. One vivid demonstration of the persistent uncertainties in Southern Ocean modeling is given by Dutay et al. (2002) in the context of anthropogenic tracer uptake by the ocean.

The present paper follows a line of publications (Speer et al. 2000a; Gordon et al. 2000; Delworth et al. 2002; Kiehl and Gent 2004; Roberts et al. 2004, etc.) in which the ability of coupled ocean–atmosphere models to perform long-term global climate simulations is assessed with a strong focus on the modeled ocean circulation. Our specific contribution lies in documenting the performance of a “hybrid” but primarily isopycnal ocean model whose architecture differs markedly from that of models traditionally used in climate simulation. This work addresses concerns raised in the latest IPCC report (Houghton et al. 2001, Sect. 7.1.3) about the low genetic diversity of today's ocean models compared to that of atmospheric models. Diversity in model design is one of the very few

---

S. Sun (✉)  
NASA Goddard Institute for Space Studies,  
New York, NY, USA  
E-mail: ssun@giss.nasa.gov

R. Bleck  
Los Alamos National Laboratory,  
Los Alamos, NM, USA

*Present address:* R. Bleck  
NASA Goddard Institute for Space Studies,  
New York, NY, USA  
E-mail: rbleck@giss.nasa.gov

**Table 1** Bottom pressure in the 20 layers of the GISS Atmospheric General Circulation Model

Layer	1	2	3	4	5	6	7	8	9	10	
Pressure (hPa)	984	964	934	884	810	710	550	390	285	210	
Layer	11	12	13	14	15	16	17	18	19	20	Top
Pressure (hPa)	150	110	80	55	35	20	10	3	1	0.3	0.1

means available for assessing the contribution of numerical errors to climate prediction uncertainty.

The principal design element of isopycnal coordinate models, in relation to conventional  $z$  coordinate models, is that depth (alias layer thickness) and density trade places as dependent and independent variables.<sup>1</sup> This switch does not affect the number of prognostic equations, nor does it alter the familiar mix of wave modes and processes by which information is transmitted in the ocean. This is to say that both model types solve the same physical problem. However, since the two models are based on different sets of differential equations, their numerical properties may be expected to be very different as well.

Studies by Boville and Gent (1998), Hirst et al. (2000), and Gent et al. (2002) show improvements in many respects in CGCM results when the GM eddy parameterization scheme (Gent and McWilliams 1990) is incorporated into the ocean submodel. Isopycnal ocean models, which have a potential advantage as far as water mass conservation is concerned because advection and lateral eddy diffusion in such models take place along isopycnal surfaces, can incorporate the GM scheme quite elegantly through interface smoothing. However, “potential advantages” of this kind may not automatically translate into higher model skill because isopycnal models are no less sensitive to physics parameterization details than the mainstream  $z$  coordinate models. “Tuning” is therefore equally labor-intensive and time-consuming for both model classes, and this is a process in which  $z$  coordinate models have a two-decade head-start. Nevertheless, the isopycnal, and especially the hybrid-isopycnal ocean model has now reached a degree of maturity that warrants documenting details of climate simulations obtained with it, even if such documentation points out the need for further model improvement.

In this study, we describe results from so-called unforced experiments in which greenhouse gas concentrations are held constant with time. These experiments are referred to as base or control runs, later to be compared with experiments in which atmospheric greenhouse gas concentrations vary with time. The model setup is described in Sect. 2. In Sect. 3, we present details of the mean state, model drift and decadal variability in multi-century simulations. Concluding remarks are made in Sect. 4.

## 2 Model description

The coupled model, referred to here as the GISS–HYCOM climate model, is one of several coupled models

developed at GISS, all sharing the same AGCM. An earlier version of this particular model combination was described in Sun and Bleck (2001a) and Sun and Hansen (2003). Since then, all three major components—atmospheric, ocean, and ice model—have undergone extensive modifications. The newly assembled model shows improvements in many respects compared to the previous version.

### 2.1 Atmospheric model

The atmospheric submodel (Schmidt et al. 2005) is based on model SI2000 (Hansen et al. 2002) and incorporates numerous improvements in basic physics including a new cloud parameterizations with subgrid convection and a new turbulence calculation in the planetary boundary layer.

The horizontal resolution in this simulation is  $4^\circ \times 5^\circ$ , but its effective resolution is shown to be somewhat higher (Russell and Lerner 1981) with the quadratic upstream differencing scheme (Prather 1986), and in at least some fields the model’s fidelity compared to observations is similar to that of the T42 Max Planck Institute model (Boyle 1998). In addition, results obtained at this resolution are found to be comparable to those with a doubled resolution of  $2^\circ \times 2.5^\circ$  (Schmidt et al. 2005), although other studies (e.g., Stratton 1999; Pope and Stratton 2002) have shown that many aspects of atmospheric simulations improve as horizontal resolution increases. Given our limited computational resources, we chose this relatively coarse horizontal resolution in order to carry out century-scale integrations within a reasonable amount of time.

Vertical resolution has been increased from 12 to 20 levels and the top of the atmosphere has been extended to 0.1 hPa, compared to 10 hPa in the previous version. There are two extra layers near the surface as well as in the lower stratosphere, and four extra layers above 10 hPa. The coordinate pressure levels are shown in Table 1.

Note that the GISS AGCM physics is “tuned” with the observed sea surface temperature (SST) to achieve near-zero heat flux balance at the surface when atmospheric composition is fixed at the level of 1880. The version of the AGCM that achieved this was then coupled to several ocean components without further tuning of AGCM-specific parameters. This strategy is certainly beneficial for an intercomparison project focusing on the role of different ocean submodels. It has, however, deprived us of the freedom to improve results by tuning the coupled model.

<sup>1</sup>Throughout this paper, the terms density, isopycnal, and temperature stand for *potential* density, isopycnal, and temperature.

**Table 2**  $\sigma_2$  Target values for the 16 layers in HYCOM, and minimum thickness of layers relegated to the  $z$  coordinate subdomain

Layer	1	2	3	4	5	6	7	8
$\sigma_2$	30.90	31.87	32.75	33.54	34.24	34.85	35.37	35.80
Min dz	20.0 (KT) 5.0(KPP)	5.0	7.6	9.8	11.6	13.0	14.0	14.6
Layer	9	10	11	12	13	14	15	16
$\sigma_2$	36.15	36.43	36.65	36.82	36.95	37.05	37.13	37.20
Min dz	14.9	15.0	15.0	15.0	15.0	15.0	15.0	15.0

## 2.2 Ocean model

We use HYCOM (Bleck 2002), the hybrid coordinate version of the Miami Isopycnal Coordinate Ocean Model, as the ocean component. The model maintains isopycnal coordinate representation in the oceanic interior but allows coordinate layers to become constant-depth layers poleward of the location where their “target” isopycnals outcrop. As shown later in Fig. 6, the hybrid coordinate framework thereby maintains vertical resolution in unstratified water columns where a purely isopycnal model would fail to provide resolution. The guaranteed presence of a fixed number of coordinate layers (16 in this case) allows vertical mixing in HYCOM to be simulated in  $z$  coordinate model fashion as a columnar diffusion process. This sets HYCOM apart from its predecessor MICOM (Bleck et al. 1992) whose architecture requires the use of a bulk Kraus–Turner surface boundary layer supplemented by convective adjustment and background interior mixing schemes. Parameterizing mixed layer processes in terms of vertical eddy diffusion is generally considered superior to relying on Kraus–Turner type turbulent kinetic energy closure. The results shown in this article bear this out.

Target densities for the 16 coordinate layers are prescribed in terms of  $\sigma_2$  (potential density referenced to 20 MPa) and are shown in Table 2. Note that the target value for layer 1 is relevant only for density-oriented post-processing of model output since layer 1 is always maintained as a constant-thickness layer in the model. Table 2 also gives the prescribed minimum thickness  $dz$  of layers falling into the non-isopycnal subdomain.

The heat flux at the surface was found to be very sensitive to the depth of the uppermost coordinate layer; the value of 20 m was chosen in experiments using the Kraus–Turner mixed layer model because it resulted in a relatively small net heat flux. This sensitivity to near-surface vertical resolution, which is usually not detected in  $z$  coordinate models because their architecture does not encourage treating vertical grid spacing as a free parameter, needs to be studied further.

HYCOM is configured in the coupled model with a horizontal mesh size of  $2^\circ \times 2^\circ \cos(\text{latitude})$ , yielding a grid cell size of  $222 \times 222 \text{ km}^2$  at the equator and  $111 \times 111 \text{ km}^2$  at  $\pm 60^\circ$  latitude in line with the cosine dependence. To avoid a zero grid size near the North Pole, the Mercator grid at  $58^\circ \text{ N}$  smoothly connects to a bipolar grid patch (Arfken 1970) whose two poles are placed in Canada and Siberia, as shown in Fig. 1. The resulting cell size at the North Pole is roughly  $60 \times 60 \text{ km}^2$ . The Bering Strait is closed in the current suite of experiments.

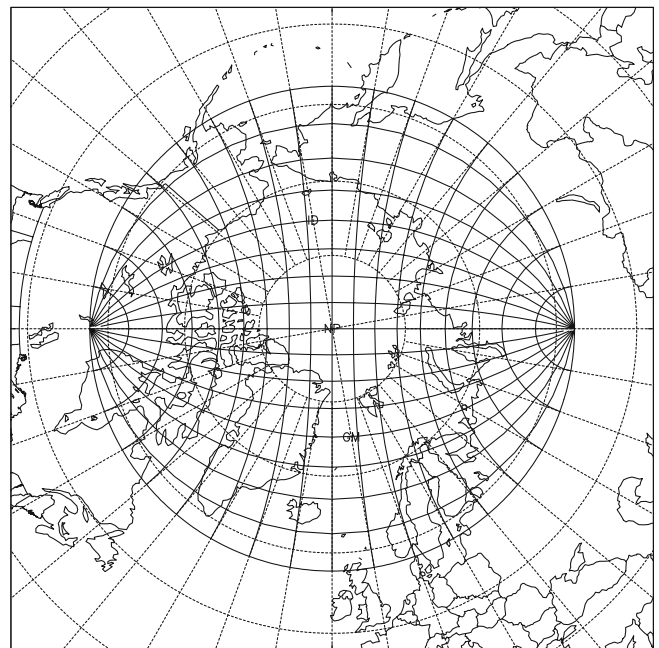
The bottom topography is obtained by spatially integrating ETOPO5 data of  $5'$  spatial resolution over each grid cell, without further smoothing. This procedure generally leads to a widening of passages and a reduction of sill depths. Since the depth of the sill, rather than its width, is found to control the flow near Iceland (Wadley and Bigg 1996), we have increased the sill depth of the Greenland–Iceland–Scotland ridge to a minimum of 798 m. The Indonesian Passage is also narrowed in order to bring its width on the coarse mesh closer to reality.

Horizontal eddy viscosity is defined as the greater of  $0.2(\text{ms}^{-1}) \times \text{meshsize}$ ,

and

$$0.3 \times |\text{DEF}| \times (\text{meshsize})^2,$$

where  $\text{DEF} = [(u_x - v_y)^2 + (v_x + u_y)^2]^{1/2}$  is the total deformation (Smagorinsky 1963). In weakly sheared flow, the resulting viscosity in the  $2^\circ$  mesh varies between  $10,000 \text{ m}^2 \text{ s}^{-1}$  near the pole and  $40,000 \text{ m}^2 \text{ s}^{-1}$  near the equator. These values are small compared to those used in other coarse-mesh models, but the gap narrows in strong shear zones where  $\text{DEF}$  takes over. Laplacian interface smoothing is done with a coefficient of 0.002

**Fig. 1** The bipolar grid

( $\text{m s}^{-1}$ ) $\times$ meshsize, resulting in values in the range 100–400  $\text{m}^2\text{s}^{-1}$ . Eddy diffusivity is set to 0.02 ( $\text{m s}^{-1}$ ) $\times$ meshsize, which puts it in the 1,000–4,000  $\text{m}^2\text{s}^{-1}$  range.

According to Sokolov et al. (2003), the early GISS–HYCOM model was among the vertically most diffusive of 13 coupled models tested. Since the isopycnal sub-domain in HYCOM by definition is essentially free of vertical numerical diffusion, the source of this large diffusion had to be the so-called grid generator which moves layer interfaces vertically to restore target density where possible and at the same time enforces minimum layer thickness constraints. Two changes were made to the grid generator to lessen its diffusive side effects:

- Instantaneous restoration of target density, occasionally requiring large layer thickness changes, was replaced by a gradual interface nudging process aimed at restoring target density on a 2-day time scale.
- The vertical “remapping” of dependent variables following each vertical “regridding” step, which originally was formulated as vertical advection based on the donor-cell or piecewise constant method (PCM), was changed to advection by the piecewise linear method (PLM).

These measures have reduced the effective vertical diffusion in the latest GISS–HYCOM version to 2.5  $\text{cm}^2\text{s}^{-1}$ , down from 5  $\text{cm}^2\text{s}^{-1}$  in the previous version (Sokolov, private communication). This factor-of-two improvement, while seemingly modest, does eliminate a major part of the spurious numerical diffusion in the model. Given that buoyancy-driven overturning circulations contribute to the effective vertical diffusion as defined by Sokolov et al. (2003), a diffusion value much smaller than 2.5  $\text{cm}^2\text{s}^{-1}$  would likely be a sign of an anemic overturning circulation.

In this paper we show results from three experiments which differ mainly in the numerical implementation of vertical mixing processes in HYCOM. The specific differences between the three model variants are as follows.

### 2.2.1 Model variant A

The model uses three different routines to handle vertical mixing, all inherited from MICOM:

1. A Kraus–Turner slab surface mixed layer model (Kraus and Turner 1967; Bleck et al. 1992);
2. An instantaneous convective adjustment scheme;
3. A diapycnal diffusion scheme for the stratified interior (McDougall and Dewar 1998).

The diapycnal diffusivity ( $\kappa_\mu$ ) depends on the local static stability after Gargett (1984):

$$\kappa_\mu = \frac{c}{N} = \frac{c}{\left(-\frac{g}{\rho_0} \frac{\partial \rho_2}{\partial z}\right)^{1/2}},$$

where  $c = 3 \times 10^{-7} \text{ m}^2\text{s}^{-2}$ ,  $\rho_0$  is a reference density, and  $\rho_2$  is the potential density referenced to 20 MPa.

The vertical remapping of dependent variables by the grid generator is based on PCM.

### 2.2.2 Model variant B

This model differs from variant A in three respects:

1. Vertical remapping of dependent variables by the grid generator is based on PLM.
2. The traditional strategy in MICOM/HYCOM of treating density  $\rho$  and salinity  $S$  as prognostic variables during advection while inferring temperature  $T$  from  $\rho$  and  $S$  is replaced by a scheme in which density and spiciness (a variable orthogonal to density in  $T, S$  space) are being advected while  $T$  and  $S$  are inferred from the former at the end of each advection step. To simplify the recovery of  $T$  and  $S$ , spiciness is linearized, i.e., reduced to a linear combination of  $T, S$ . For details, see Bleck (2005).
3. A “poor man’s” plume model is used to dispose of brine expelled during the freezing of sea water. In previous model versions, the expelled salt was added to the surface mixed layer, occasionally increasing its density to the point where convection would set in. The subsurface warmer water brought to the surface by the convection would then melt the ice, often in a way that would distribute the meltwater over a relatively thick mixed layer. Given the near-impossibility of forming ice on top of a convectively unstable deep layer (the Polynia effect), no new ice would form during the remainder of the winter season. Furthermore, since an ice-free ocean does not receive meltwater for restoring the surface halocline in spring, the ice loss tended to be permanent. This phenomenon has previously been described by Kim and Stössel (2001).

To overcome the above problem, we make the rather extreme assumption that the expelled brine becomes organized in plumes that acquire sufficient negative buoyancy to descend to depths greater than 500 m. We make the additional assumption that these plumes do not exchange properties with the ambient waters till they pass the 500 m mark. This approach to plume modeling is similar to, though slightly simpler than, a scheme proposed by Duffy et al. (1999). While indefensible in its details, it allows the model ocean to remain convectively stable underneath newly formed ice, thereby preserving the ice until springtime when surface heating not only melts the ice but also reduces the mixed layer depth, the latter being a prerequisite for forming of a strong seasonal halocline near the surface. This halocline, in turn, is essential for determining the outcome of the race between polynia and ice formation in the following fall season in favor of ice formation.

The above treatment helps the model retain more ice in the Southern Ocean, as shown later in Fig. 7. Because the modeled seasonal changes in Southern Ocean ice coverage are relatively small, the “brine pump” effect is



actually quite limited in model variant B. In cases with a stronger seasonal cycle of ice coverage in the Southern Ocean, the “brine pump” tends to be too active and then acts as a primary source for deep water formation, as discussed below. Physically more sound implementations of the plume model are available (e.g., Paluszkiwicz and Romea 1997; Stössel et al. 2002; Canuto et al. 2004) and will be incorporated into HYCOM in the near future.

The above model variant A and B were used for the Fourth IPCC assessment named GISS-EH and GISS-EH2, respectively.

### 2.2.3 Model variant C

This model is identical to variant B, except:

1. The three mixing modules listed under variant A are replaced by the K Profile Parameterization (KPP) scheme (Large et al. 1994; Halliwell 2004), with the non-local mixing effect included.
2. The “brine pump” is weakened as it appears to lead to excessive rates of dense water generation. Instead of uniformly distributing salt between 500 and the bottom, salt expelled during the freezing of sea water in run C is distributed evenly over the uppermost 1,000 m, or the total water depth, if it is shallower than 1,000 m.
3. The coefficient governing lateral  $T/S$  diffusion is enhanced sixfold in the equatorial grid row and fourfold and twofold in the rows one and two grid points away from the equator, respectively. The intent is to capture the diffusive effect of tropical instability waves which are not adequately resolved on the  $2^\circ$  mesh. Without this enhancement, advection along the equator extends the cold tongue too far to the west. We will return to this point later.

### 2.3 Sea ice model

A sea ice dynamics model based on the Hibler viscous-plastic rheology (Zhang and Rothrock 2000) has been added to a four-layer thermodynamic ice model (Russell et al. 2000). The ice model is configured on the AGCM grid and is, in fact, treated as part of the AGCM to sharpen the focus of the GISS model intercomparison on the performance of the various ocean components. However, as in many coupled models, the OGCM has a finer resolution than the AGCM. Carrying the sea ice model on the AGCM grid therefore is likely to reduce the fidelity of the ice simulation. This issue will have to be addressed in the future.

### 2.4 Land surface and precipitation runoff

There are four surface types in the GISS AGCM: open water, ice-covered water, ground and glacier. The vertical fluxes in each atmospheric grid cell are area aver-

ages over each surface type. The land surface and soil hydrology model is described in Friend and Kiang (2005).

River runoff is incorporated by accumulating the net freshwater input at each land point and, if positive, directing it to a designated ocean grid box according to the slope of the local topography. Glacier ice melting is prescribed as a constant 0.01 Sv around Greenland and 0.064 Sv around Antarctica (Schmidt et al. 2005). Since these numbers are kept constant with time, they are a potential source of global freshwater imbalance.

### 2.5 Flux coupler

The model components are coupled as follows. The OGCM provides SST, sea surface salinity (SSS) and rate of ice formation to the AGCM, and receives surface fluxes of heat, freshwater, momentum and salt (from melting sea ice) from the AGCM. This information exchange is handled by a flux coupler and takes place at 4-h intervals, thereby partially resolving the diurnal cycle. (The time step for the AGCM and OGCM is 30 min and 1 h, respectively.) The flux coupler interpolates fields between the different grids of the model components while conserving area averages of property fluxes. The SST sent to the AGCM represents an average over the area enclosed by each AGCM grid cell; surface fluxes sent to the OGCM are spatially integrated in analogous fashion. Both fluxes and the state variables are averaged over the coupling time interval.

No surface flux adjustments have been used in these experiments. With more climate modeling groups making efforts to eliminate such adjustments, see for example the third Hadley Centre Coupled OAGCM (HadCM3, Gordon et al. 2000) and the NCAR CSM (Boville and Gent 1998), we continue the no-flux and no-spinup approach used in Woods et al. (1999) and Sun and Bleck (2001a).

Due to the fact that the atmospheric and ocean model have different horizontal resolutions, the coastlines in the two model grids do not match. To assure conservation of interface fluxes during mapping, we let the model with finer horizontal resolution (in this case the ocean model) designate the coastline of the coupled model. As a result, some grid cells in the atmospheric model are partially water and partially land cells.

### 2.6 Initial conditions

The atmospheric initial state is described in Schmidt et al. (2005). Atmospheric composition is set to the so-called pre-industrial level, a term referring to conditions prevailing around 1880. This composition is held constant during the control experiment which is the topic of the present article. The ocean model starts with temperature and salinity based on Steele et al. (2001) in the Arctic, Levitus Climatology (1994) in the rest of the

ocean, and zero oceanic velocity. Initial ice coverage and thickness are described in Schmidt et al. (2005).

It is debatable whether emphasis in climate modeling should be placed on minimizing initial transients in coupled runs or on starting a climate forecast with initial conditions that closely match the observed ocean state. As already stated, we presently lean toward the latter alternative and therefore omit separate ocean spinup runs.

### 3 Model results

A 500-year control run of model A and B has been completed while the control run of model C has finished 250 years at the time of this writing. For ease of comparison, we present results at year 250 unless noted otherwise.

The discussion of model results will be structured around the following main themes: (1) model drift; (2) surface flux features; (3) thermohaline overturning circulation; and (4) ENSO variability. We will focus on results from runs B and C as there are many similarities between runs A and B. Results from run A will be shown only when notable differences occur.

#### 3.1 Model drift

Figure 2 illustrates the adjustment of the horizontally averaged  $T$ ,  $S$  fields in run B in a  $z$  coordinate reference frame over the course of the 500-year integration. The prominent features are (a) cooling in the upper 1,000 m by as much as  $-1.8^{\circ}\text{C}$  at 100 m depth; (b) a generally positive salinity drift reaching values as high as  $0.3 \text{ g kg}^{-1}$  at depths between 10 and 100 m, and (c) warming in the deeper ocean by as much as  $0.8^{\circ}\text{C}$  near 4,000 m.

Figure 3, which shows the  $T/S$  deviation from the initial conditions in latitude-depth space in run B at year

250, reveals that upper-ocean cooling is largely confined to the tropical and subtropical warm-water lens, with values as high as  $-5^{\circ}\text{C}$  in a  $50^{\circ}$  wide belt centered on the equator. This is the latitude belt occupied by the upwelling limb of the two subtropical shallow overturning cells. Judging from the near-discontinuity of isallotherms at 20 m depth, the cooling is a consequence of insufficient downward mixing of the warm surface waters by our HYCOM-specific implementation of the Kraus–Turner mixed layer. (The Kraus–Turner closure approach is ideal for layer models in which a coordinate interface can be chosen to coincide with the bottom of the mixed layer. Since HYCOM is allowed to switch to  $z$  coordinate representation near the surface, this advantage is lost, requiring numerical compromises.)

Figure 3 also suggests that the positive salinity trend in the 100–1,000 m depth range is due to subduction of midlatitude water which in both hemispheres is slightly saltier than observed. Less obvious is the connection between the gradual warming trend in the deep ocean and any particular anomaly in subducted-water properties. At least part of the deep-sea warming seen in Fig. 2 appears to be associated with the substantial warming of the water column at extreme southern latitudes seen along the left edge of Fig. 3. A similar warming in run A (not shown) is what led to the adoption of the “brine pump” countermeasure in run B.

The sharp transition between warming south of  $60^{\circ}\text{N}$  and cooling north of there seen in Fig. 3 is shown in Fig. 4 to be associated with two geographically distant events, namely, surface warming in the northwest Atlantic, brought about by a westward shift of the North Atlantic Drift Current, and marked cooling in the Norwegian Sea. The westward shift of the NADC is one of the classical problems of coarse-mesh ocean models.

Isallohalines in the northern North Atlantic in Fig. 3 are consistent with the warming/cooling dipole just described, in the sense that thermal SST anomalies tend to spawn evaporation anomalies that make anomalously warm (cold) water anomalously salty (fresh).

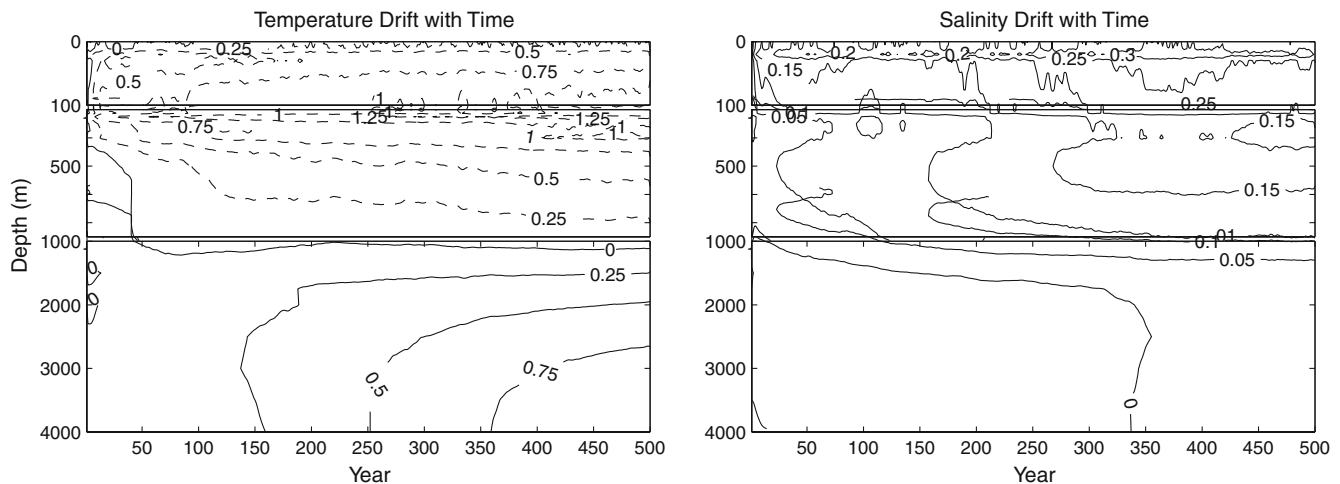
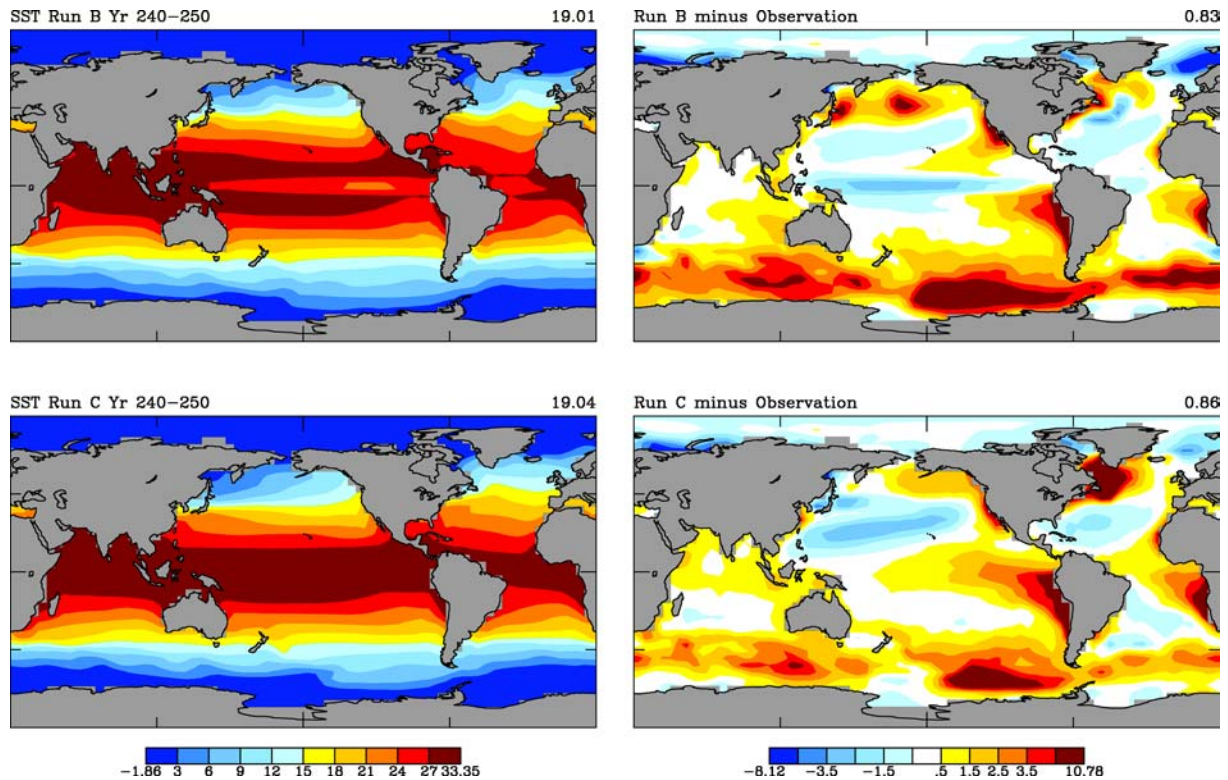
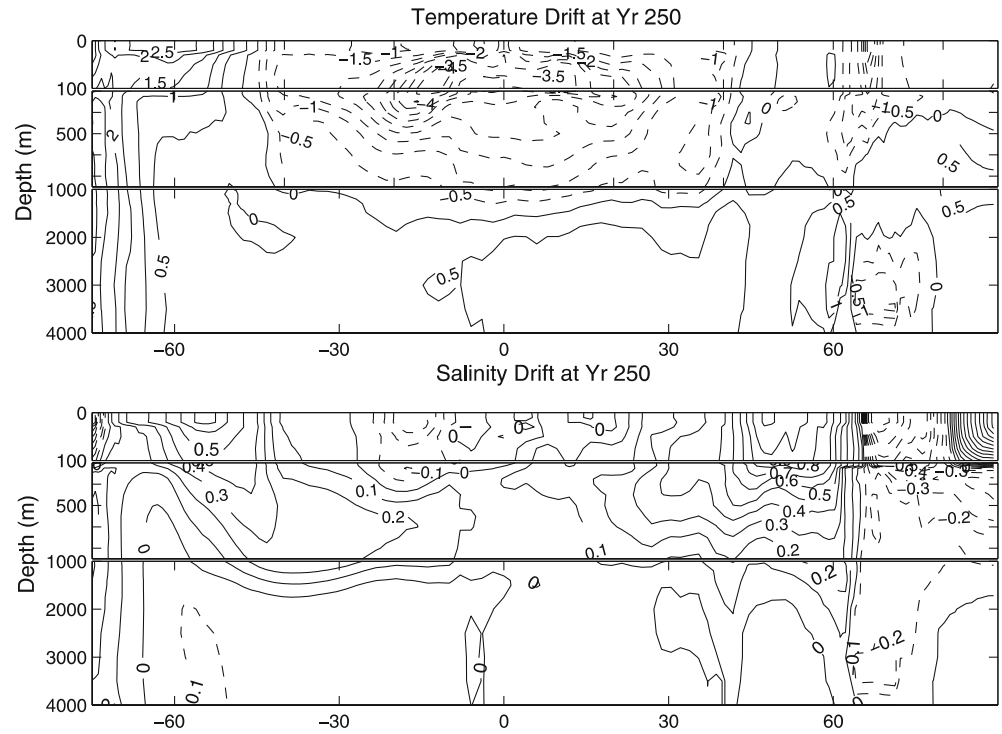


Fig. 2 Horizontally averaged temperature ( $^{\circ}\text{C}$ ) and salinity (psu) drift during 500 years in run B

**Fig. 3** Zonally-averaged temperature ( $^{\circ}\text{C}$ ) and salinity (psu) deviation from annual Climatology at year 250 in run B



**Fig. 4** Sea surface temperature (*left*) and its deviation from annual climatology (*right*) for runs B (*top*) and C (*bottom*) at year 240–250

An illustration of long-term changes in stratification from an isopycnal coordinate viewpoint is provided in Fig. 5 in the form of time series plots of isopycnal layer thickness. For the purpose of this display, the

archived  $T/S/dz$  fields have been converted to density space, i.e., the thicknesses shown are those which a coordinate layer would have if its density matched its target density.

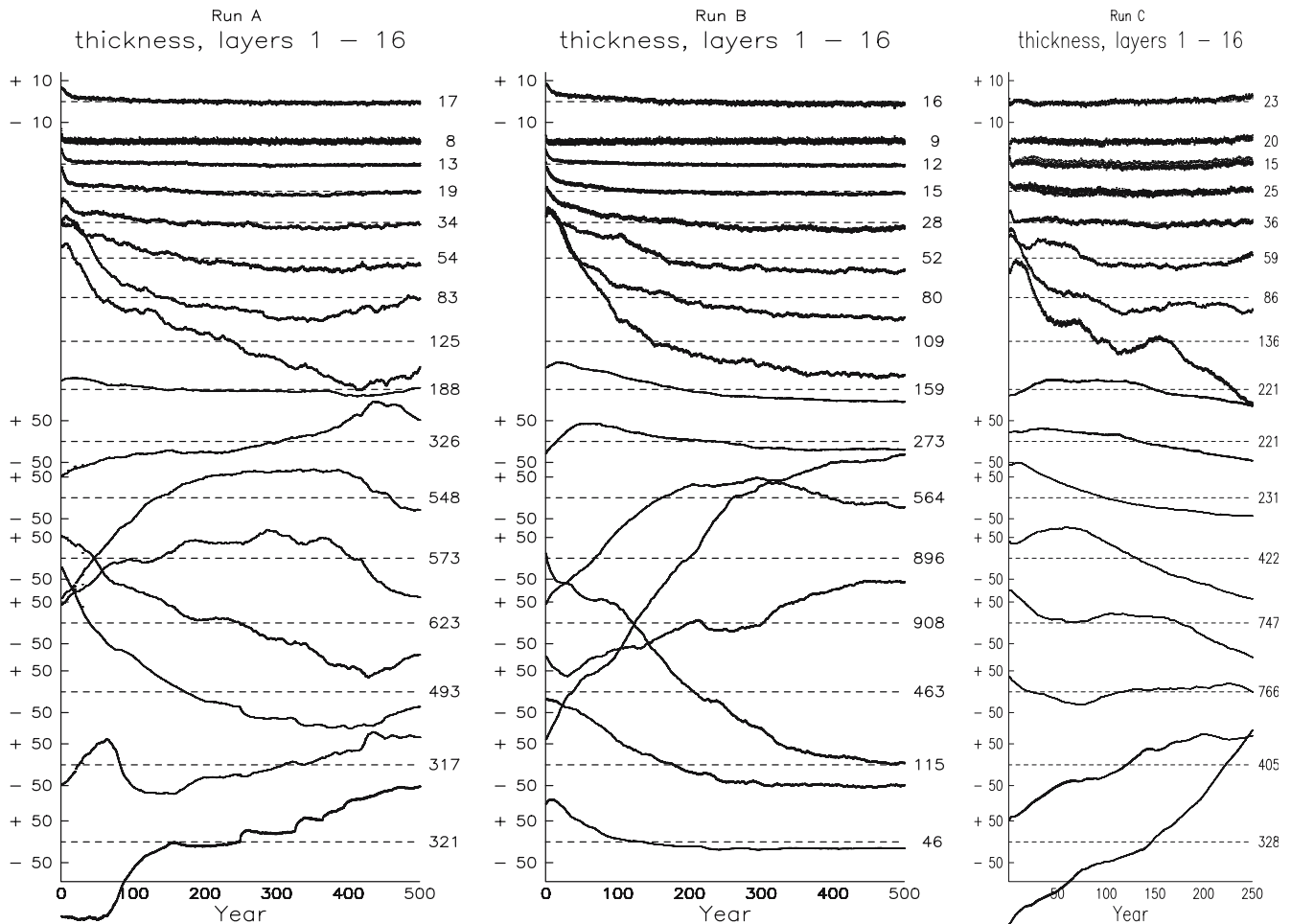


**Fig. 5** Drift of horizontally-averaged isopycnal layer thickness ( $m$ ) relative to temporal mean for 16 layers in runs A (left), B (center), and C (right). Some ordinate labels omitted to avoid crowding. Numbers on the right indicate temporal mean

The main message conveyed by Figs. 2 and 5 is that internal adjustment of the ocean is by no means completed at year 500. Judging from Fig. 5, isopycnal layer thicknesses adjust somewhat more strongly in run B than in run A, and the drift displayed in depth-time space, as in Fig. 2, turns out to be smaller in run A (not shown) than run B.

The zonally averaged layer distribution (*not* converted to density space, thus revealing the actual transition from isopycnal to  $z$  coordinate subdomain in the model) is displayed in the left column of Fig. 6 for runs B and C. The layers are seen to be isopycnal over most of the interior ocean. Only in the high-latitude surface ocean, where the low target densities assigned to the uppermost coordinate layers do not exist, do layers turn into constant depth layers.

The most prominent difference between the two left-hand panels of Fig. 6 is the buildup of dense water at high southern latitudes in run C. This buildup is reflected in the sharp rise of layer 16 thickness seen in the lower right corner of Fig. 5.

The right-hand panels of Fig. 6 highlight the temporal trend in zonally averaged stratification in runs B

and C, again from an isopycnal perspective. Whereas in run B the ocean is getting warmer everywhere except in the low-latitude warm-water lens (similar to what was seen in Fig. 3), run C shows widespread cooling at depths greater than 1,000 m.

An important integrator of model drift caused by surface flux imbalances is sea ice coverage. The ice extent in the three runs is shown in Fig. 7, with the observed seasonal excursions marked by dashed lines. In the northern hemisphere, all runs have good winter ice coverage, which is about  $12.5 \times 10^{12} \text{ m}^2$  according to observations. In summer, however, ice extent is almost twice as high as the observed value of  $5 \times 10^{12} \text{ m}^2$ , indicating too weak a seasonal cycle. The ice extent in the southern hemisphere decreases dramatically during the first 30 years in runs A and B, and hardly recovers after that. Compared to the observed range of  $3 \times 10^{12} \text{ m}^2$  in summer to  $15 \times 10^{12} \text{ m}^2$  in winter (dashed lines), the ice coverage during winter is far too low, again resulting in a weak seasonal cycle. One model feature that contributes to the loss of ice is the spurious open-ocean convection in the Southern Ocean, as previously discussed. The rudimentary plume model removing brine from the



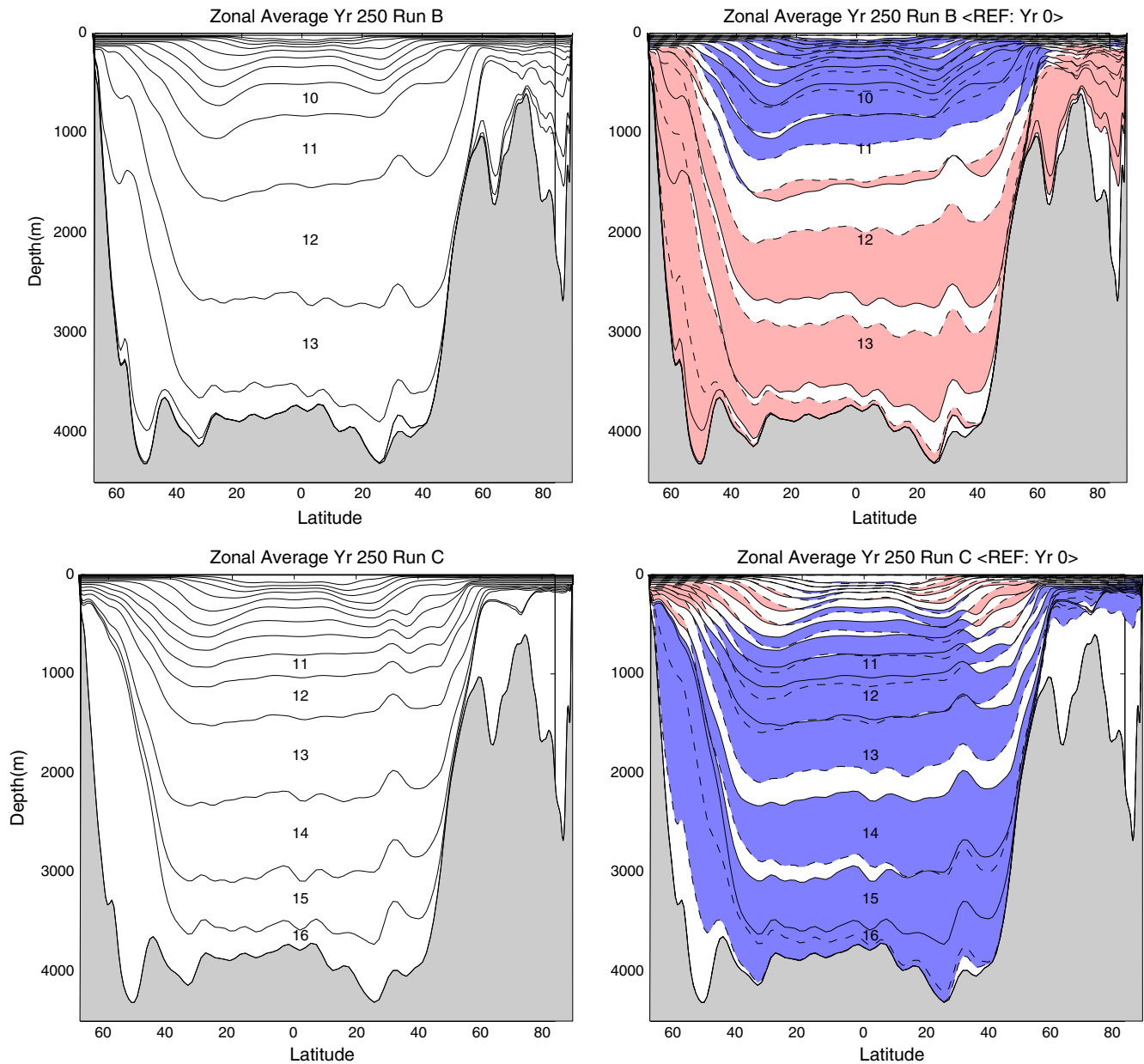


**Fig. 6** Left Zonally averaged cross section showing hybrid layer interfaces in run B (top) and in run C (bottom), both at year 250. Layer indices are marked in the middle of each layer. Right Isopycnal interface depths shown at left overlaying interface depths

at year 0 in run B (top) and run C (bottom). Red/blue shading indicates downward/upward interface displacement, associated with warming/cooling

surface layer in run B is able to partially reduce this ice loss. It is the substitution of the KPP mixed layer scheme for the Kraus–Turner and convective adjustment schemes, however, which in run C brings southern ice extent into agreement with observations.

Note that there are several peaks in northern ice coverage in run A. These are caused by treating  $\rho$  and  $S$  as prognostic variables while diagnosing  $T$  at the end of each advection step. With cold water density being mainly a function of  $S$ , diagnosing  $T$  becomes a poorly constrained and hence error-prone operation at high latitudes. Under certain conditions, mainly related to

stratification anomalies preventing detrainment of water from the Kraus–Turner mixed layer, the error can amplify and lead to a fictitious “cold source” which is responsible for the episodes of excessive ice growth seen in run A in Fig. 7. The problem is eliminated by substituting spiciness for salinity as prognostic variable during the advection process, as mentioned in Sect. 2.2.2(2).

To round out the discussion of model drift, we show in Fig. 8 time series of global mean ocean temperature and salinity, as well as horizontally averaged SST and SSS, for the three runs. In runs A and B, the global mean

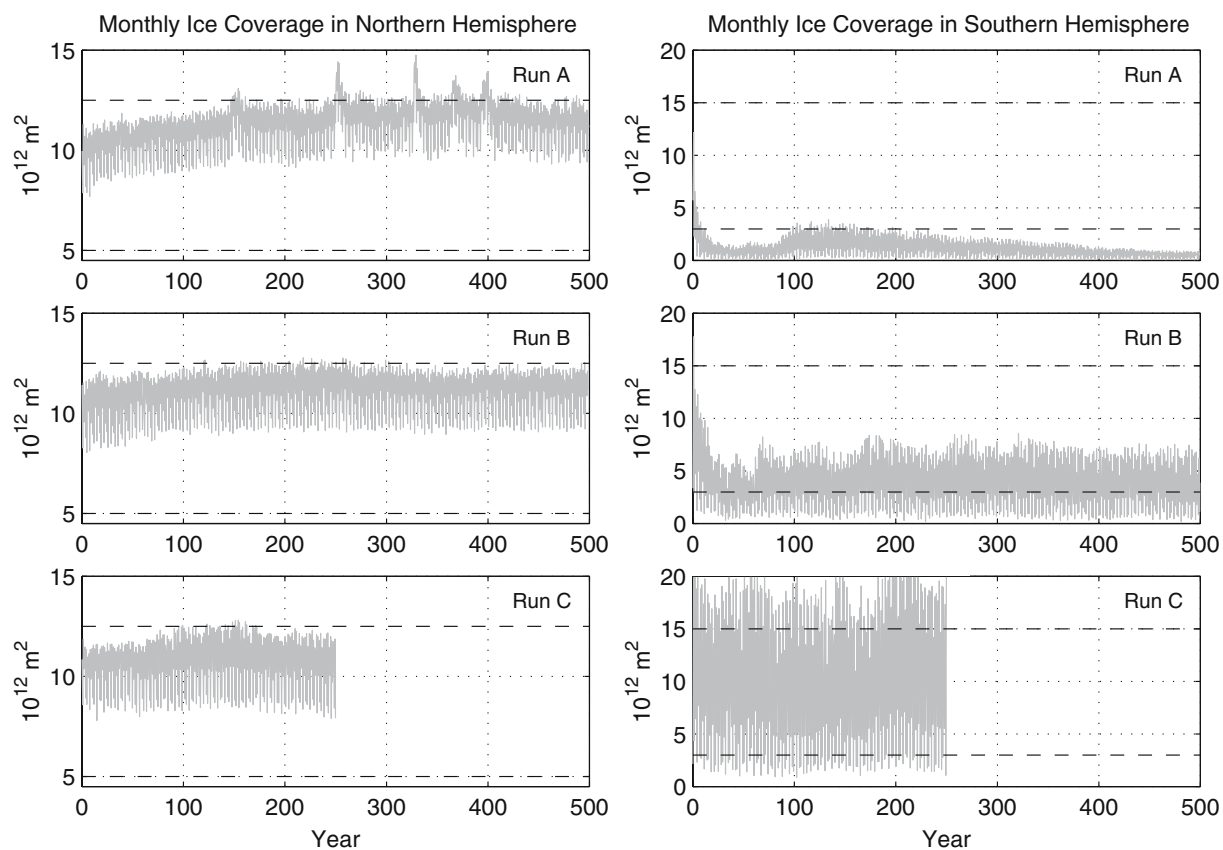


**Fig. 7** Time series of sea ice extent in both hemispheres in runs A (*top*), B (*center*), and C (*bottom*). Dashed lines mark the seasonal range in observations

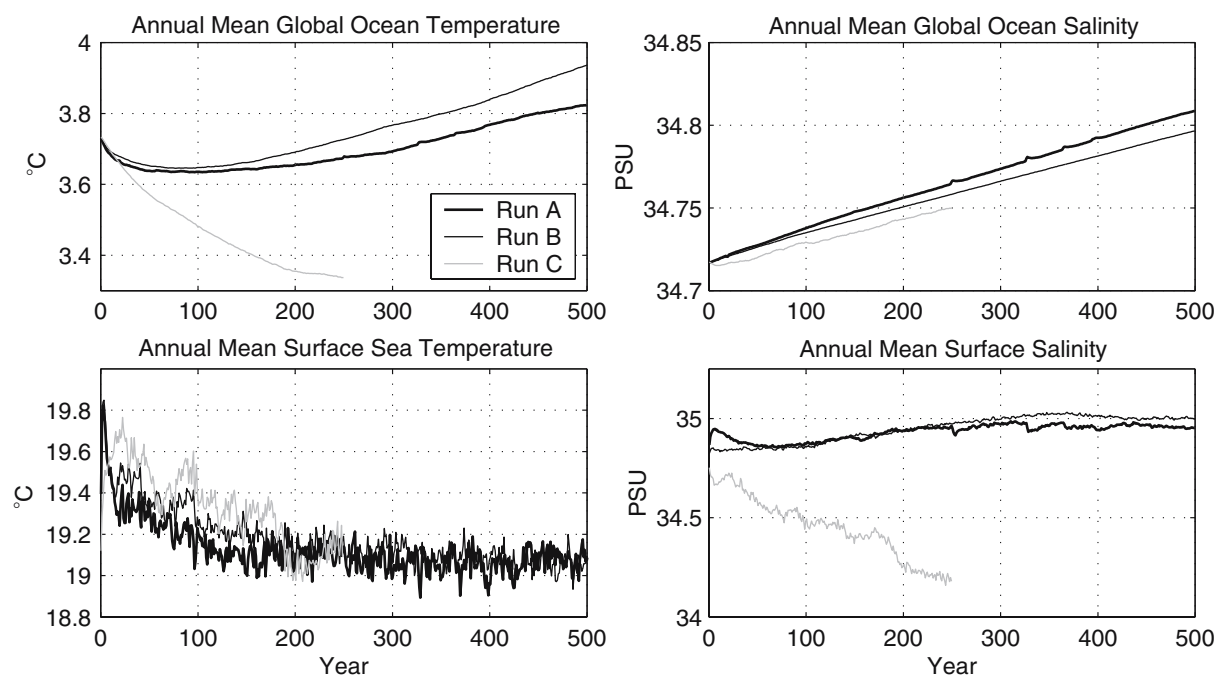


**Fig. 8** Time series of annually averaged global ocean temperature/salinity and sea surface temperature/salinity in runs A, B, and C

temperature decreases by almost  $0.1^{\circ}\text{C}$  in the first 50 years. Following that is a much slower warming trend. The cooling is also apparent in the SST in the first 100 years, but SST remains relatively steady thereafter. The global salinity has a constant positive trend of  $0.02\text{ g kg}^{-1}$  per century in runs A and B. This may be related to the fact that the freshwater flux in HYCOM is converted into a virtual salt flux proportional to the local salinity, and thus the total amount of salt in the ocean is not guaranteed to be conserved. Note that the gradual freshening of the surface ocean in run C modifies the salt flux and results in a smaller drift in global salinity.

Run C behaves quite differently from the other two runs in terms of temperature as well. While the SST appears to stabilize during the second century, the ocean as a whole continues to cool. The cooling trend is consistent with a long-term heat loss at the surface of roughly  $1\text{ W m}^{-2}$ , to be further discussed in the following Section.

### 3.2 Air–sea fluxes

From the climate prediction perspective, the ocean/ice model plays a seemingly limited role: it provides two fields—SST and sea ice coverage—which are needed to set the lower boundary conditions for the atmospheric model. (The effect of surface currents on momentum transfer between ocean and atmosphere is generally ignored, i.e., wind stress is computed under the assumption that the ocean is at rest.) Details of the ocean circulation are therefore relevant only if they affect SST and ice coverage. However, an erroneously modeled ocean circulation can do severe damage to a climate simulation because of the ocean’s huge heat capacity, which allows it to expose the atmosphere or cryosphere to unrealistic temperatures for long periods of time.

As pointed out earlier in this paper, the sea ice model in GISS–HYCOM is configured on the atmospheric grid. Hence, the two fields needed for computing lower boundary conditions for the atmosphere in this particular model combination are SST and the heat flux needed to keep the ocean from cooling below the freezing temperature of sea ice.

In the following sections we compare surface fluxes computed by the atmospheric boundary layer module in GISS–HYCOM to observations.

#### 3.2.1 Surface heat flux

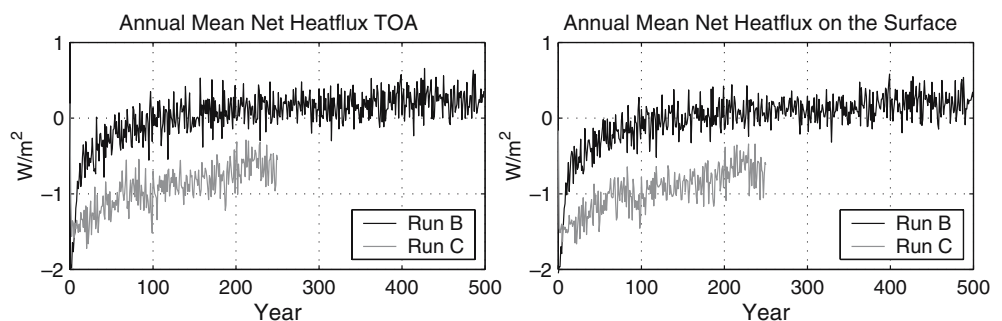
As stated earlier, the GISS AGCM is “tuned” to be in radiative balance when driven by the observed SST and fixed atmospheric composition of 1880. When it is coupled to HYCOM, the global surface heat flux initially is negative (upward), indicating that the global ocean surface warms up quickly. However, Fig. 9 shows that by year 30 the net heat flux in run B, both at the surface and at the top of atmosphere, is within  $\pm 0.5\text{ W m}^{-2}$ .

While the KPP scheme in run C leads to a dramatic improvement in southern ice coverage, it does not allow the ocean to settle into a state of zero net heat flux as quickly as runs A and B. One facet of run C that may help explain the steady  $1\text{ W m}^{-2}$  global heat loss indicated in Fig. 9 is the elevated SST in the tropics and subtropics (lower left panel in Fig. 4), related to weaker-than-observed equatorial surface currents and upwelling. At first sight, the place in the ocean most affected by this steady heat loss is the bottom coordinate layer which, according to the right panel of Fig. 5, steadily gains mass at the expense of several lighter (and presumably warmer) layers above. However, we will argue later that this conspicuous mass buildup in layer 16 is mainly driven by vertical salt flux.

We see here an example of the extraordinary sensitivity of the ocean–atmosphere system to physical closure assumptions, and of the tradeoffs in model bias typically encountered when replacing one parameterization of unresolved processes by another.

The meridional distribution of zonally- and time-averaged net surface heat flux, as well as its four components—absorbed shortwave radiation, net longwave radiation, latent heat, sensible heat—are shown in Fig. 10 for runs B and C averaged over years 240–250. Also shown in this figure are (1) the corresponding quantities from the GISS AGCM climatology; (2) observations compiled at the Southampton Oceanography Centre (Josey et al. 1999); and (3) an observational dataset obtained by combining the GSSTF2 dataset for latent and sensible heat flux (Chou et al. 2003; Roma-

**Fig. 9** Time series of net annual mean heat flux (positive down) at the top of atmosphere and at the surface in runs B and C



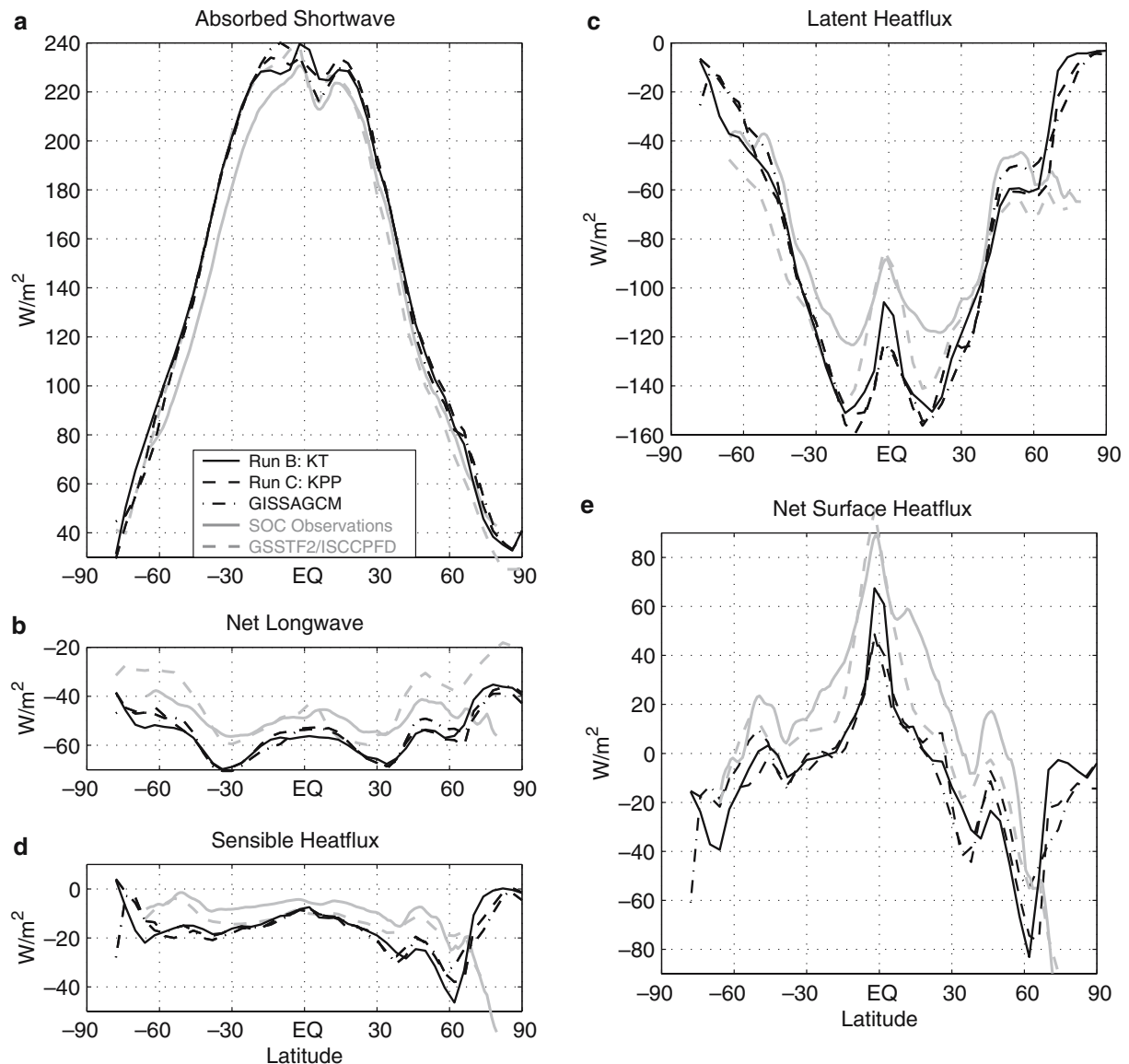


**Fig. 10** Annually and zonally averaged absorbed shortwave, net longwave, latent, sensible and net heat flux (positive down) in runs B and C, GISS AGCM climatology, observations from SOC, and

observations from GSSTF2/ISCCP-FD. Spatial averaging extends over ice-free and ice-covered ocean

nou et al. 2005) with the ISCCP-FD dataset for longwave and shortwave radiation (Zhang et al. 2004). All five panels have the same vertical scale for easy comparison. Discrepancies between model and observations are apparent in all four components, the biggest discrepancy being in the latent heat flux near the equator. (Note, however, the disconcerting spread in the observational estimates of latent heat flux in that latitude range.) As a result, the net downward heat flux in the tropics is smaller in the model than observed. In general, all four flux components in runs B and C are closer to the GISS AGCM climatology than to observations. The biggest discrepancy among model runs is in the latent heat flux at the equator due to the aforementioned difference in the extent and strength of the Pacific cold tongue between runs B and C.

Note that in the tropics all model runs produce a latent heat flux that is too strong compared to observations. This is true not only for run B with a cold SST bias and run C with a warm SST bias, but also for the stand-alone GISS AGCM with prescribed SST (Fig. 10c). The available evidence points at the AGCM as the likely source of this flux bias.

The horizontal distribution of net heat flux at the surface is shown in Fig. 11. The downward heat flux in the tropics appears to be smaller in all models than in the observations. The heating of the Pacific and Atlantic equatorial cold-water tongues in runs B and C is limited to a narrow latitudinal band which in run B extends too far west with little zonal variation, most noticeably in the Pacific. The difference between runs B and C in heat uptake along the equator is one major factor contrib-



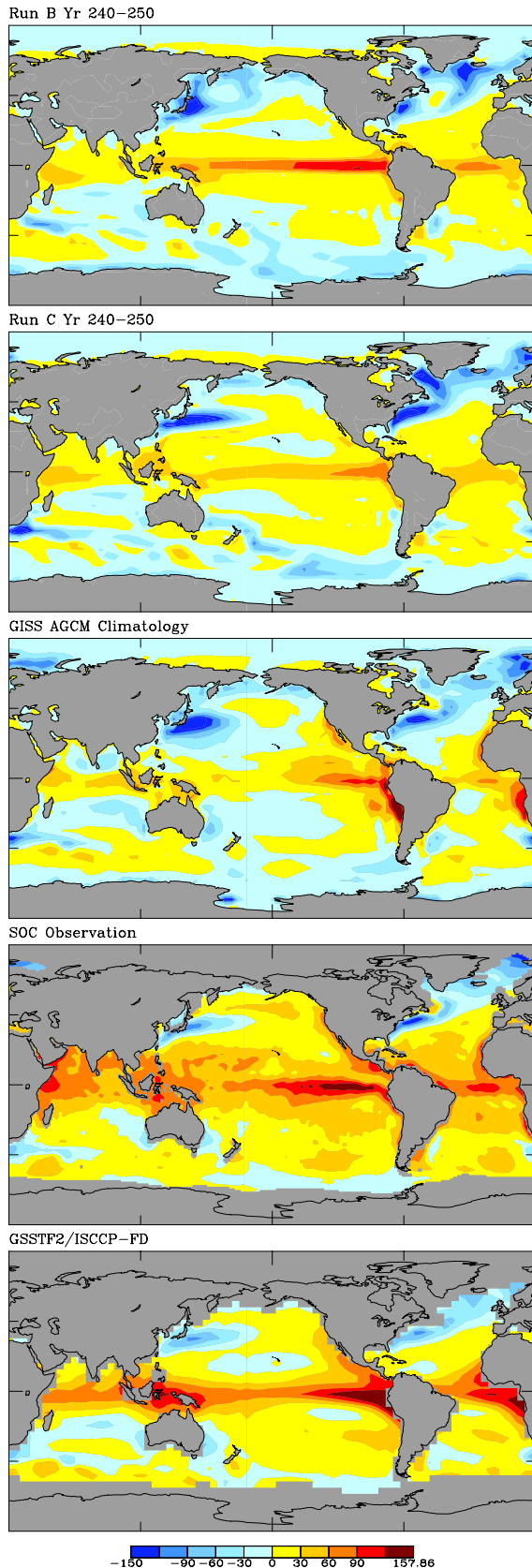


**Fig. 11** Annually averaged net surface heat flux ( $\text{W m}^{-2}$ , positive down) from runs B and C, GISS AGCM climatology and observations from SOC and GSSTF2/ISCCP-FD

uting to the global net heat flux imbalance shown in Fig. 9.

In the extratropical regions, the geographic distribution of net heat flux in runs B and C shares a high degree of similarity with GISS AGCM climatology.

### 3.2.2 Surface freshwater flux and wind stress

Zonal mean precipitation and evaporation fields as well as their sum are shown in Fig. 12 for runs B and C, the GISS AGCM climatology, and observations from SOC (Josey et al. 1999) and GPCP (Huffman et al. 2001). Run B has two precipitation maxima at  $10^\circ$  north and

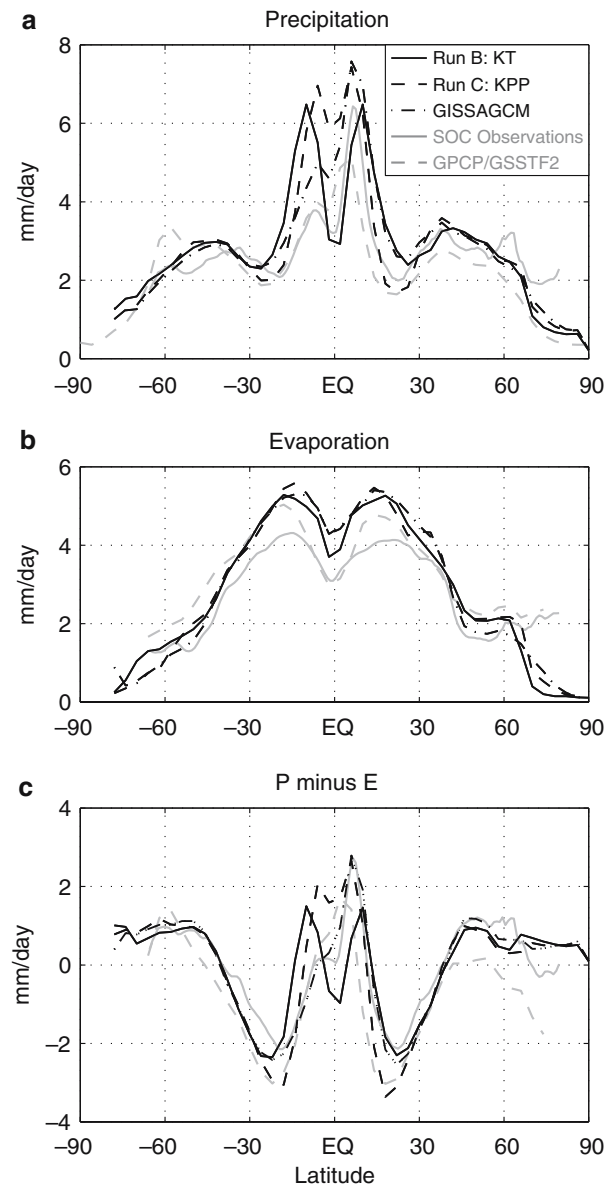


**Fig. 12** Zonal mean precipitation, evaporation, and the sum of the two ( $\text{mm day}^{-1}$ ) over ocean, in runs B and C, GISS AGCM climatology, and observations from SOC and GPCP/GSSTF2

south of the equator, and a minimum in-between. Similar patterns occur in run C, although the minimum is less pronounced. Overall in the tropical region, both precipitation and evaporation appear to be stronger in the model than in the observations. The net freshwater flux is therefore closer to observations than its two components individually—as one would expect given the limited capacity of the atmosphere to store excess water vapor.

The horizontal distribution of the precipitation for the five cases in Fig. 12 is shown in Fig. 13. An unrealistic double precipitation maximum created by a double InterTropical Convergence Zone is seen in run B with a distribution that is too zonal compared to observations. The excessive westward extent of the equatorial precipitation minimum is a consequence of the elongated cold-water tongue. The boomerang-shaped Pacific precipitation pattern in run C is much closer to reality, in line with the different SST distribution shown in Fig. 4.

Failure to correctly model the suppression of the southern ITCZ is a long-standing problem in climate modeling (e.g., Delworth et al. 2002; Kiehl and Gent 2004). It is generally attributed to the inability of the AGCM to resolve the blocking effect of the Andes Cordillera, leading the model to underestimate the meridional wind component along the South American coast which in nature is responsible for strong coastal upwelling. The resulting warm bias of the modeled Humboldt Current and its low-latitude zonal extension prominently displayed in the right-side panels of Fig. 4 allows the coupled model to develop a southern ITCZ during austral summer.

For future reference, we also plot the zonal mean eastward and northward wind stress in Fig. 14 for runs B and C, GISS AGCM climatology and observations from SOC and GSSTF (Chou et al. 2003). The model results generally are in good agreement with the observations, except at high latitudes where the modeled eastward wind stress tends to be too weak and the northward component too strong.

### 3.3 Vertical-meridional overturning

Thermohaline-forced overturning circulations capable of ventilating the deep ocean, thereby lifting deep water to the surface and exposing it to the atmosphere, have a major effect on the climate. They are, in fact, the main reason why decadal- to century-scale climate prediction must be carried out with a 3-dimensional “dynamic” ocean model reacting to the gamut of thermal and haline atmospheric forcing.

Vertical-meridional overturning circulations are typically displayed in terms of stream functions in depth-latitude space, obtained by integrating the meridional flow component at different depths zonally across individual ocean basins. To gain additional insight into the connection between meridional overturning and

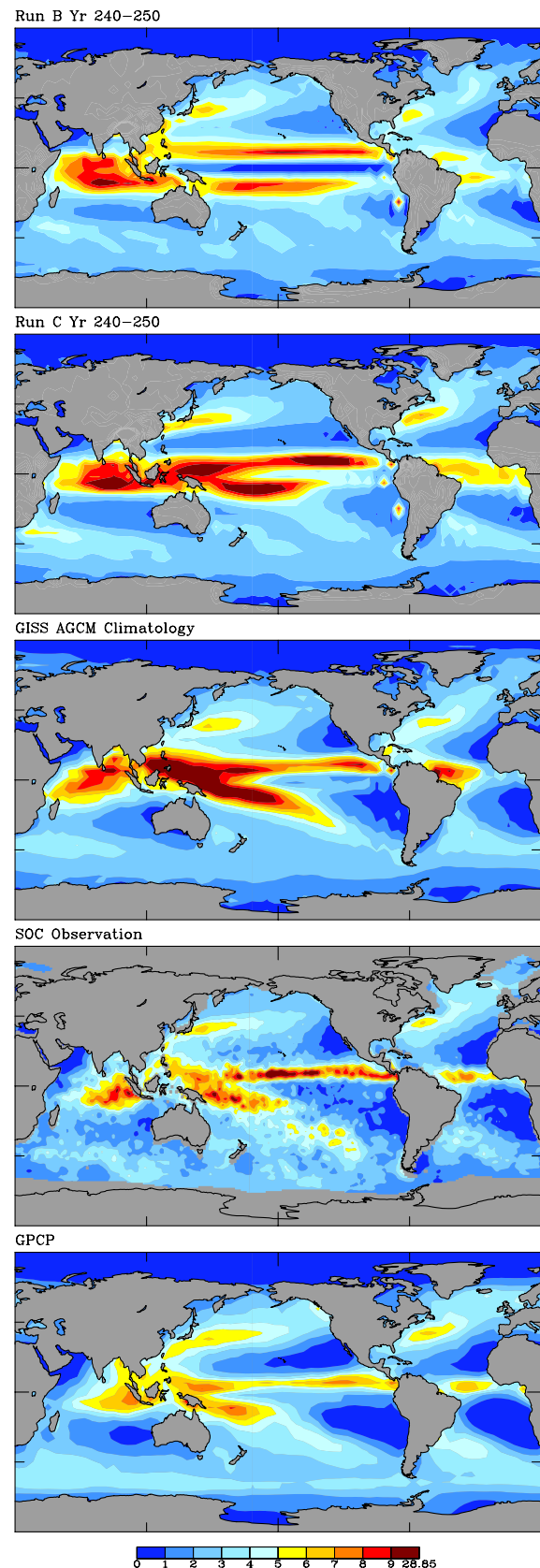


**Fig. 13** Annual mean precipitation ( $\text{mm day}^{-1}$ ) from runs B and C, GISS AGCM climatology and observations from SOC and GPCP

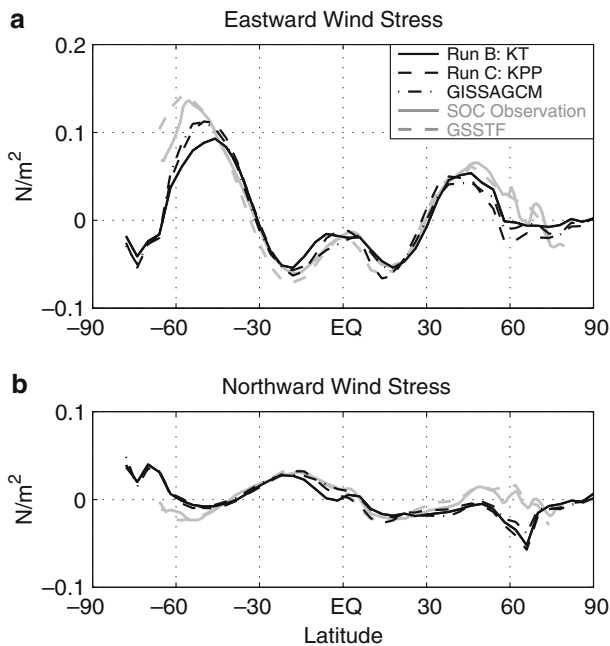


**Fig. 14** Zonal mean eastward and northward wind stress over ocean ( $\text{N m}^{-2}$ ) in runs B and C, GISS AGCM climatology, and observations from SOC and GSSTF

meridional heat flux, the overturning stream function is sometimes transformed and displayed in density-latitude space (Hirst and McDougall 1997; Speer et al. 2000a; Talley et al. 2003). With HYCOM being a predominantly isopycnal coordinate model, the density-latitude stream function is particularly straightforward to generate.

The meridional overturning stream function averaged over 10-year periods in runs A,B,C is shown in Fig. 15 for the Atlantic, Indian, Pacific and the global ocean. Horizontal mass fluxes in HYCOM's  $z$  coordinate surface layers were transformed into isopycnal fluxes prior to zonal summation. This transformation is important as it eliminates the part of the thermally indirect Deacon cell in the Southern Ocean which arises from flux averaging in  $z$  space (Speer et al. 2000b).

As shown in the leftmost column of Fig. 15, the Atlantic overturning rate from three runs ranges from about 18 to 23 Sv. The stream function maximum is found near  $50^\circ\text{N}$  at the bottom of layer  $\sigma_2 = 36.82$  whose average depth, according to Fig. 5, is 1,700 m for run B and 1,050 m in run C.

The modeled overturning rate during the chosen 10-year period is in agreement with the data-based estimate of Talley et al. (2003), who arrive at a maximum rate in the Atlantic of 18 Sv, occurring at isopycnal values of  $\sigma_2 = 36.90$ , and at a depth of 1,200 m. The northward flow of AABW seen in the Talley et al. results is too weak in the model to reach the North Atlantic.

In the Pacific, the circulation is dominated by two shallow cells symmetric to the equator, driven by wind-forced equatorial upwelling, and a cell representing deep

water from the Southern Ocean entering the Pacific. (Rudimentary equatorial cells are also seen in the Atlantic.) The northern near-surface cell is much shallower in run C than in runs A and B. All three cells are slightly stronger than in Talley et al. (2003).

Much of the deep water from the Southern Ocean upwells into lighter layers in the Pacific basin, presumably due to interior diapycnal mixing, and a significant portion returns to the Southern Ocean at intermediate densities. The upwelling rate of deep Pacific water to the surface at the equator varies among 10, 0, and 4 Sv in runs A, B and C, respectively, compared to 6 Sv in the Talley et al. (2003) analysis.

About 5, 4, and 1 Sv of deep water from the Southern Ocean enters the Indian Ocean and upwells near the equator in runs A, B and C, respectively.

The Southern Ocean in run A is dominated by a strong thermally direct cell of roughly 36 Sv. This cell is driven by unrealistically strong heat loss from the largely icefree Southern Ocean. The additional ice cover in runs B and C prevents such large amounts of heat from escaping and thereby reduces the southern cell to 16 and 10 Sv, respectively. The surface flux-driven 10 Sv cell in run C is shallow by comparison and is complemented by a separate 26 Sv subsurface cell encompassing the lowest four model layers.

We see here the far-reaching effects of the brine convection scheme which, by reducing excessive open-ocean convection, significantly narrows the gap between model results and observations as far as surface-driven overturning is concerned. The price paid for eliminating unrealistic convection in run C is the generation of a strong near-bottom cell driven by salt export from the surface.

The reduced strength of the southern cell in runs B and C allows the interhemispheric cell driven by North Atlantic downwelling to extend into the southern hemisphere and connect to the wind-forced northward surface flow in the  $50\text{--}60^\circ\text{S}$  latitude belt. This is particularly noticeable in run C where the split of the southern cell seen in runs A and B into a shallow surface-driven one and a deep brine-pump driven one allows the interhemispheric cell to extend to the sea surface. The interhemispheric scope of the North Atlantic overturning cell agrees qualitatively with observations (Talley et al. 2003).

In order to calculate smoothly varying individual stream functions for the Pacific and Indian Ocean, the source/sink introduced by the Indonesian throughflow has been compensated in Fig. 15 by adding a clockwise circulation around Australia equal and opposite to the throughflow.

Information about the geographic layout of the meridional overturning circulation can be obtained by diagnostic tools originally developed for the work presented in Sun and Bleck (2001b) and described in detail in Bleck and Sun (2004). Figure 17 shows, for runs B and C, the diapycnal flux through interfaces chosen to coincide with the depth of maximum Atlantic over-

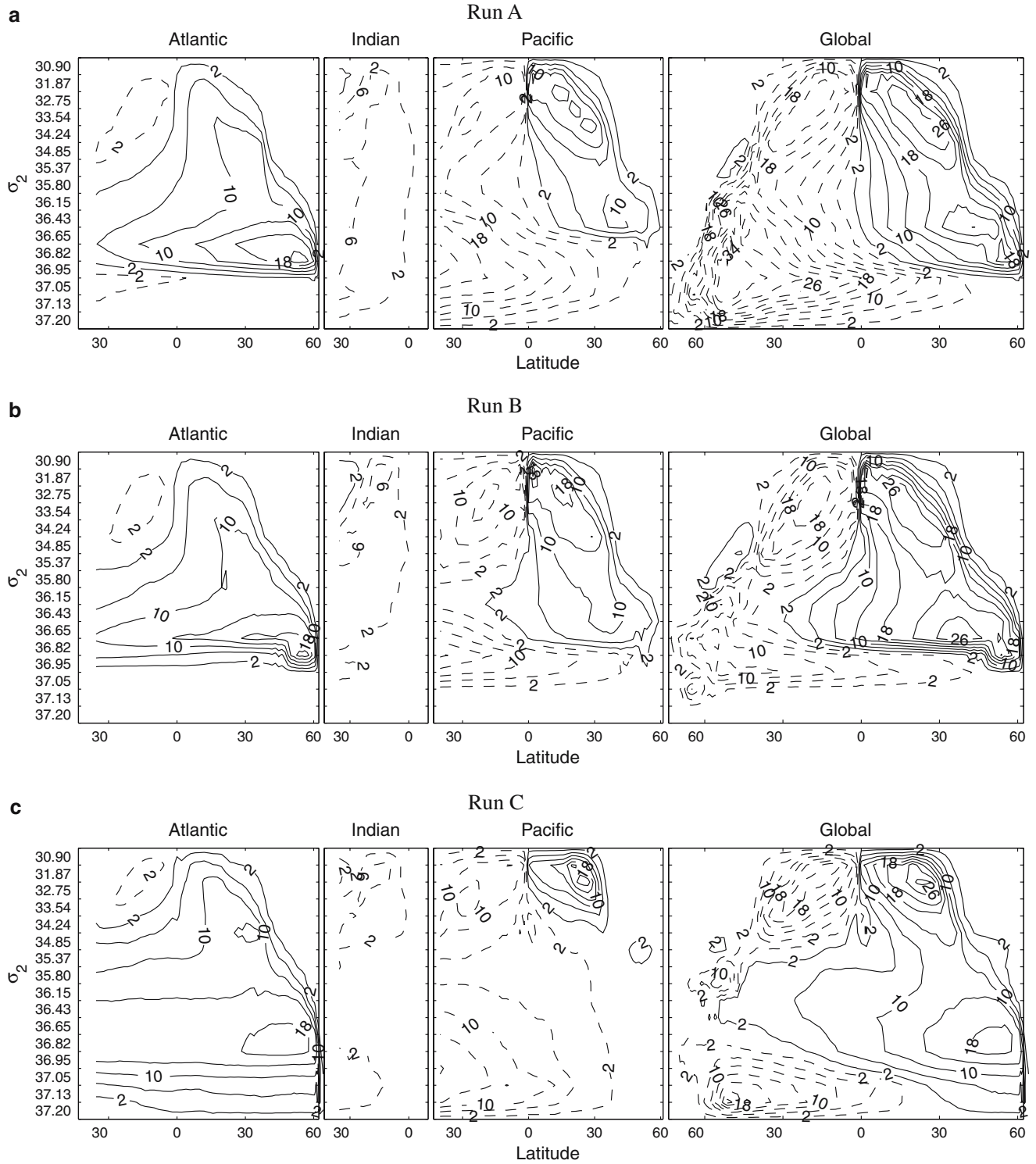


**Fig. 15** Overturning stream function in the global ocean and three individual basins as a function of latitude and  $\sigma_2$  for runs A, B and C

turning in Fig. 15b, c. respectively. The diapycnal motion is displayed in two ways, namely, in terms of diapycnal vertical motion (in units of  $\text{m year}^{-1}$ ) and in terms of diapycnal mass fluxes (in units of Sv), the latter associated with individual patches of up- or downward motion.

In run B, most of the North Atlantic downwelling (22 Sv strong) is seen in Fig. 17 to take place over the south flank of the Greenland–Iceland–Scotland ridge. Downwelling in the Greenland–Iceland–Norwegian Sea is insignificant by comparison. The geographic distribution of downwelling in run C conforms more closely





arctic Circumpolar Current, yields a sizable net amount, roughly 27 Sv, of Pacific upwelling into the  $\sigma_2 = 36.65 \text{ kg m}^{-3}$  layer from below. The corresponding upwelling numbers in the Atlantic and Indian Ocean basins add up to 12 and 3 Sv, respectively. In run C, the upwelling numbers are 2, 8, and 0 Sv in the Atlantic, Pacific and Indian, respectively.

One major difference between the two panels of Fig. 17 is in the Southern Ocean where the up- and downwelling flux numbers for run B add up to a net 11 Sv downward flux, consistent with Fig. 15b, while there is no diapycnal motion to speak of in run C. As indicated earlier, the absence of thermohaline surface forcing allowing relatively light surface water in the Southern Ocean to sink to great depths represents a major improvement of run C over the earlier runs.

A large range of ocean heat transport from coupled models is seen in Jia (2003). The northward heat transport from GISS–HYCOM in three basins as well as the global basin is shown in Fig. 16. A comparison of the top two panels shows that the partial recovery of southern ice in run B, seen in Fig. 7, plays an important role in reducing the excessive southward heat transport in the Southern Ocean in run A. Heat transport curves in runs B and C broadly correspond to those obtained by the NCEP reanalysis (Trenberth and Caron 2001).

Heat flux calculations only make sense in situations of zero net mass flux. To arrive at separate heat fluxes for the Indian and Pacific Ocean in Fig. 16, the method used in Fig. 15 was invoked again, that is, a clockwise circulation around Australia was added carrying the same amount of mass and heat as is flowing through the Indonesian passage.

We conclude this section by showing in Fig. 18 the variation with time of several parameters that are traditionally used to assess the general “health” of the modeled global circulation. The gradual strengthening of the Atlantic overturning circulation in run B during the years 200–300 (top panel) is due to a density increase in the North Atlantic. The middle panel gives values for the mass transport through the Drake Passage for run B which compare favorably to the observed estimates of  $123 \pm 11$  Sv (Whitworth and Peterson 1985) and  $134 \pm 11.2$  Sv (Cunningham et al. 2003), while run C exhibits a stronger throughflow. The strength of the Drake Passage transport is set by a complex interplay of buoyancy forcing, wind forcing, and bottom drag (Olbers et al. 2004). We surmise that the large transport in run C is linked to the extra baroclinicity (steepening of isopycnal layers) resulting from the accumulation of layer-16 water next to the Antarctic continent. This trend can easily be seen by comparing the upper and lower panels in Fig. 6.

The modeled strength of the Indonesian throughflow is estimated to be around 15 Sv in both run B and C, as shown in the bottom panel of Fig. 18. This number is on the high side of the observed range of  $[-2, 18]$  Sv given by Fieux et al. (1996). The throughflow rate is set by the wind stress and relative strength of upwelling in the

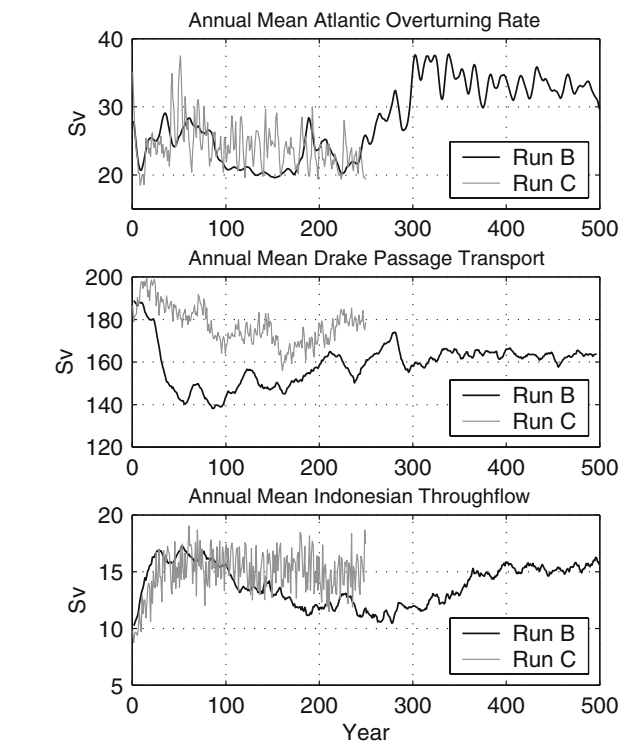


Fig. 18 Time series of annual mean Atlantic overturning rate (top), Drake Passage transport (center) and Indonesian throughflow (bottom) in runs B and C

Indian and Pacific basin. For a given wind stress pattern, it likely depends on the relative magnitude of diapycnal mixing in the two basins.

### 3.4 ENSO variability

The El Niño–Southern Ocean variability is the largest multi-year natural variability mode in the coupled ocean–atmosphere system. Its underlying mechanism is fairly well understood today, even though its predictability remains an open issue. Given the need to distinguish natural from anthropogenic variability in climate forecasts, the ability of a coupled model to simulate the ENSO variability is considered a major test of the model’s abilities (Meehl et al. 2001; AchutaRao and Sperber 2002), and climate model development teams invest much effort into achieving an ENSO-like variability in their model.

We limit our discussion of ENSO to two points:

1. The GISS–HYCOM model exhibits fairly strong ENSO-like variability.
2. The amplitude of the ENSO signal is extremely sensitive to implementation details in HYCOM, such as the target density in the upper layers and the minimum thickness of layers falling into the  $z$  coordinate subdomain.

The sensitivity to vertical resolution near the surface is not totally unexpected but still perplexing in its

magnitude. As already mentioned, experimentation with vertical grid spacing is far simpler in HYCOM than in  $z$  coordinate models. As a result, this particular sensitivity, to our knowledge, has not been explored widely by the  $z$  coordinate model community.

The dependence on target density values is surprising at first but can be explained as follows. It is customary in HYCOM to set near-surface target densities unrealistically low in order to force the uppermost coordinate layers into  $z$  mode, because this simplifies the tuning of air-sea exchange processes and turbulence closure schemes in the surface mixed layer. However, as more layers are forced into  $z$  mode, the transition to isopycnal coordinate representation occurs at greater depths unless the  $z$  layers are packed more tightly. Given that material layer models are far more capable of suppressing numerical vertical diffusion than fixed-grid models, increasing the depth range occupied by the  $z$  coordinate subdomain is likely to weaken SST variability in the upwelling region of the eastern Pacific, thereby weakening the ENSO signal. [Note that the original El Niño model by Cane et al. (1986) was an isopycnal coordinate model.]

To demonstrate the sensitivity of the ENSO signal to various model parameters, we show in Fig. 19 several time series of the Niño3 index, defined as the monthly deviation of SST from the corresponding monthly climatological mean in a  $10^\circ$  wide equatorial strip extending from  $90^\circ\text{W}$  to  $150^\circ\text{W}$ . Panels 1–5 are from the last 50 years of runs B, B', C, C' and C'', while panel 6 shows the observed index for the period 1950–2000. We have introduced three new runs here as examples of extreme behavior in terms of Niño3 amplitude. Run B' is identical to run B, except that (1) its top layer minimum depth is reduced from 20 to 5 m (the value ordinarily reserved for the KPP scheme, see Table 2), and (2) it uses the enhanced equatorial lateral  $T/S$  diffusion coefficient from run C (Sect. 1). Run C' is identical to C except that it does not use the enhanced lateral  $T/S$  diffusion coefficient discussed in Sect. 1. Run C'' is identical to run C' except that it has 21 layers extending the target density range toward progressively lighter layers (and thereby spawning more  $z$  layers in the model).

Note that the two “mainstream” runs, B and C, display middle-of-the-road behavior as far as Niño3 index amplitude is concerned.

Due to the relatively large number of parameters that were varied to trigger the ENSO responses assembled in Fig. 19, the search for a simple “ordering principle” is difficult. Experimentation with this goal in mind is continuing.

#### 4 Concluding remarks

The present article describes an ongoing effort at the Goddard Institute for Space Studies to conduct centennial-scale climate prediction with a coupled model

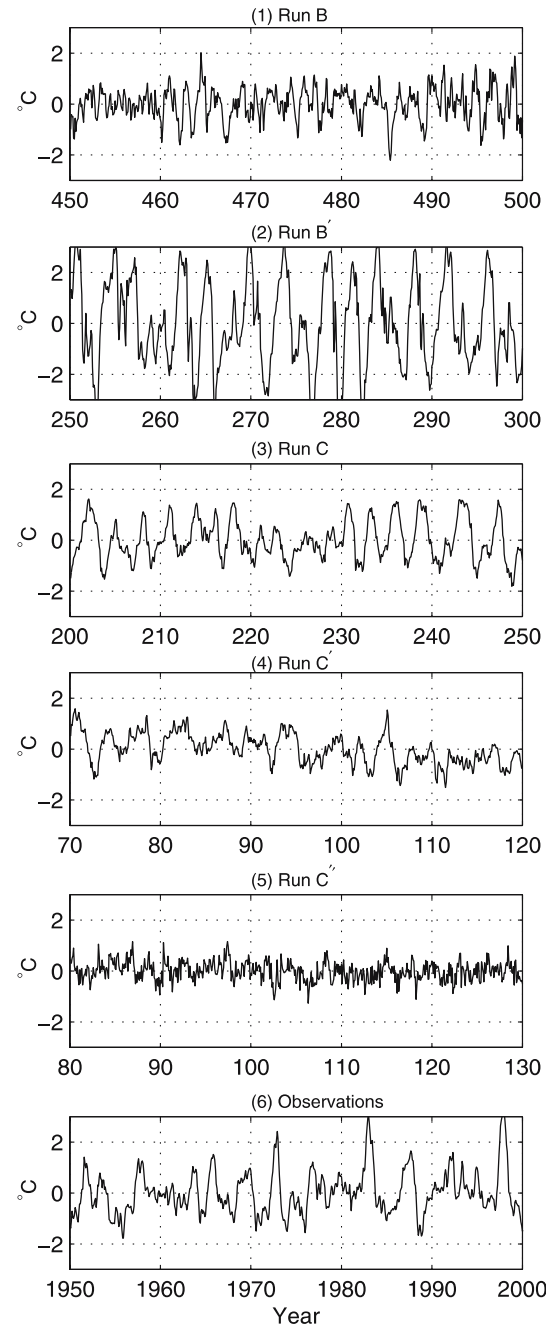


**Fig. 19** Niño3 index from the last 50 model years in runs B, B', C, C', and C'' and observations of year 1950–2000

whose oceanic component uses a hybrid (but primarily isopycnal) vertical coordinate. This project addresses concerns raised by members of the climate modeling community regarding the relatively sparse “gene pool” of ocean models used in climate prediction which may hide the true magnitude of numerics-induced model biases.

Our ocean model development work, whose latest outcome has been sketched here, retraces in many ways the efforts by other teams engaged in coupled ocean–atmosphere simulation. The realization reached in this

paper—that the breadth of ocean processes is too large to expect any particular physical closure scheme to outperform another one in *all* respects—also is not entirely new. The magnitude of the spatial truncation errors in today’s ocean models, both horizontal and vertical, is such that closure schemes developed for one particular model architecture and spatial grid need to be carefully re-tuned when used on a different grid or, worse yet, transplanted to a model that handles the resolved dynamics in a different manner. However, we have learned that re-tuning does not necessarily improve model results across the board in geographically different parts of the domain.

One case in point is the nonphysical diapycnal mixing taking place when solving transport equations discretized on an  $x, y, z$  grid. By virtue of their design, isopycnal-coordinate models are able to significantly reduce this false mixing. While we are presently unable to document the consequences of this change in any particular instance, we suspect that reduction of numerically induced diapycnal mixing “de-tunes” some of the closure schemes originally developed for  $z$  coordinate models. The strict control of vertical property fluxes in a material-layer model in particular creates profound new sensitivities to details in the parameterization of subgridscale vertical turbulent exchange. Consequently, most of the differences between model runs discussed in this paper are related to changes in surface boundary layer and deep convection closure schemes. (Similar sensitivities probably exist in the parameterization of *lateral* stirring processes, but these are even harder to document and remedy than those confined to the vertical direction alone.)

Our experience with surface mixed layer closure schemes serves to illustrate the points just made. GISS–HYCOM, equipped with the KPP scheme, shows improvements in several respects over earlier runs using a Kraus–Turner bulk mixed layer, but its global mean SST is higher than observed, resulting in a global net upward surface heat flux of  $1 \text{ W m}^{-2}$ , and therefore in a larger model drift. Judging from the net heat flux distribution with latitude (Fig. 10), this imbalance originates mostly in the tropics. Doubling the background vertical diffusivity, whose default value of  $10^{-5} \text{ m}^2 \text{ s}^{-1}$  we inherited from models discretized in  $z$  space, essentially removes the SST bias and model drift, but in the process the Niño3 variability is severely damped, a sensitivity to the vertical diffusivity also seen in Meehl et al. (2001). This suggests that KPP, although widely tested in the  $z$  coordinate framework, cannot be relied on to work in every respect in density space without renewed tuning. The sensitivity of model drift to minor model physics changes is well-known (e.g., Hirst et al. 2000), and this makes the fine-tuning of a model used for climate prediction a laborious exercise indeed.

The inclusion of sea-ice dynamics in the GISS–HYCOM model has improved sea-ice coverage, compared to the earlier version. In addition, the export of brine generated during freezing of sea water into deeper parts

of the water column, partly through the nonlocality of KPP scheme, has a big, and in this particular case well-understood, impact on water mass formation and circulation. This again demonstrates the important role of sea-ice related parameters on the simulated climate (Meehl et al. 2000).

Our presently held view is that the brine pump, based more on physical intuition than on hard observational evidence, is a transitional feature that should be phased out as soon as possible. In our most recent model experiments, salt ejected during freezing has been spread over a much shallower depth range, 50–300 m, without detrimental effects on sea ice coverage. Judging from WOCE measurements of vertical CFC penetration in the Southern Ocean (Orsi and Whitworth 2004), a plume penetration depth of a few hundred meters seems realistic. This is to say that the latest rendition of the brine pump is no longer grossly at variance with observational evidence.

Given the plethora of unintended side effects of the brine pump scheme, it is fortunate that no other major model problems have surfaced in our work that would have required similarly “engineered” solutions. (Surface flux corrections, popular in the past, arguably belong to this category.)

By analyzing circulation features in density space, we have been able to demonstrate in several instances the consequences of different turbulence closure choices for thermohaline-forced circulations whose accurate treatment is vitally important for century-scale climate prediction. Our technique for displaying diapycnal flux fields on selected isopycnals in particular leads to insight which would be difficult to gain otherwise.

**Acknowledgments** SS is supported by NASA/MIT agreement NNG04GF12A. RB was supported by the Climate Change Prediction Program in the U.S. Department of Energy’s (DOE) Office of Science. We thank G. Schmidt, J. Hansen and R. Ruedy for useful suggestions, and A. Romanou for the GPCP/GSSTF data.

## References

- AchutaRao K, Sperber KR (2002) Simulation of the El Niño Southern Oscillation: results from the Coupled Model Inter-comparison Project. *Clim Dyn* 19:191–209
- Arfken G (1970) *Mathematical methods for physicists*, 2nd edn. Academic, San Diego, p 815
- Bleck R (2002) An oceanic general circulation model framed in hybrid isopycnal-Cartesian coordinates. *Ocean Model* 4:55–88
- Bleck R (2005) On the use of hybrid vertical coordinates in ocean circulation modeling. In: Chassignet E (ed) *Proceedings of summer school of oceanography*, Lalonde, France. Kluwer, Dordrecht
- Bleck R, Sun S (2004) Diagnostics of the oceanic thermohaline circulation in a coupled climate model. *Global Planet Change* 40:233–248
- Bleck R, Rooth C, Hu D, Smith L (1992) Salinity-driven thermocline transients in a wind- and thermohaline-forced isopycnal coordinate model of the North Atlantic. *J Phys Oceanogr* 22:1486–1505
- Boville BA, Gent PR (1998) The NCAR climate systems model, version one. *J Clim* 11:1115–1130



- Boyle JS (1998) Evaluation of the annual cycle of precipitation over the United States in GCMs AMIP simulations. *J Clim* 11:1041–1055
- Cane MA, Zebiak SE, Dolan SC (1986) Experimental forecasts of El Niño. *Nature* 322:827–832
- Canuto VM, Howard A, Hogan P, Cheng Y, Dubovikov MS, Montenogro LM (2004) Modeling ocean deep convection. *Ocean Model* 7:75–95
- Chou S-H, Nelkin E, Ardizzone J, Atlas RM, Shie C-L (2003) Surface turbulent heat and momentum fluxes over global oceans based on the Goddard satellite retrievals, version 2 (GSSTF2). *J Clim* 16:3256–3273
- Cunningham SA, Alderson SG, King BA, Brandon MA (2003) Transport and variability of the Antarctic Circumpolar Current in Drake Passage. *J Geophys Res* 108(C5):8084. DOI 10.1029/2001JC001147
- Delworth TL, Stouffer RJ, Dixon KW, Spelman MJ, Knutson TR, Broccoli AJ, Kushner PJ, Wetherald RT (2002) Review of simulations of climate variability and change with the GFDL R30 coupled climate model. *Clim Dyn* 19:555–574
- Duffy PB, Eby M, Weaver AJ (1999) Effects of sinking of salt rejected during formation of sea ice on results of an ocean-atmosphere-sea ice climate model. *Geophys Res Lett* 26:1739–1742
- Dutay J-C, Bullister J, Doney SC, Orr JC, Najjar RG, Caldeira K, Campin J-M, Drange H, Follows M, Gao Y, Gruber N, Hecht MW, Ishida A, Joos F, Lindsay K, Madec G, Maier-Reimer E, Marshall JC, Matear R, Monfray P, Plattner GK, Sarmiento JL, Schlitzer R, Slater RD, Totterdell IJ, Weirig M-F, Yamanaka Y, Yool A (2002) Evaluation of ocean model ventilation with CFC-11: comparison of 13 global ocean models. *Ocean Model* 4(2):89–120
- Fieux M, Molcard R, Ilaude AG (1996) Geostrophic transport of the Pacific-Indian oceans throughflow. *J Geophys Res* 101:12421–12432
- Friend A, Kiang N (2005) Land surface model development for the GISS GCM: effects of improved canopy physiology on simulated climate. *J Clim* 18:2883–2902
- Gargett AE (1984) Vertical eddy diffusivity in the ocean interior. *J Mar Res* 42:359–393
- Gent PR, Craig AP, Bitz CM, Weatherly JW (2002) Parameterization improvements in an eddy-permitting ocean model for climate. *J Clim* 15:1447–1459
- Gent P, McWilliams JC (1990) Isopycnal mixing in ocean circulation models. *J Phys Oceanogr* 20:150–155
- Gordon C, Cooper C, Senior CA, Banks H, Gregory JM, Johns TC, Mitchell JFB, Wood RA (2000) The simulation of SST, sea ice extents and ocean heat transports in a version of the Hadley Centre coupled model without flux adjustments. *Clim Dyn* 16:147–168
- Halliwell GR (2004) Evaluation of vertical coordinate and vertical mixing algorithms in the HYbrid Coordinate Ocean Model (HYCOM). *Ocean Model* 7:285–322
- Hansen J et al (2002) Climate forcings in Goddard Institute for Space Studies SI2000 simulations. *J Geophys Res* 107(D18):4347. DOI 10.1029/2001JD001143
- Hirst AC, McDougall TJ (1997) Meridional overturning and diapycnal transport in a  $z$ -coordinate ocean model including eddy-induced advection. *J Phys Oceanogr* 28:1205–1223
- Hirst AC, O'Farrell SP, Gordon HB (2000) Comparison of a coupled ocean-atmosphere model with and without oceanic eddy-induced advection. Part I: ocean spinup and control integrations. *J Clim* 13:139–163
- Houghton JT, Ding Y, Griggs DJ, Noguer M, van der Linden PJ, Dai X, Maskell K, Johnson CA (eds) (2001) Climate change. The scientific basis. Contribution of working group I to the third assessment report of the intergovernmental panel on climate change (IPCC). Cambridge University Press, Cambridge, p 881
- Huffman GJ, Adler RF, Morrissey MM, Curtis S, Joyce R, McGavock B, Susskind J (2001) Global precipitation at one-degree daily resolution from multi-satellite observations. *J Hydrometeor* 2:36–50
- Jia Y (2003) Ocean heat transport and its relationship to ocean circulation in the CMIP coupled models. *Clim Dyn* 20:153–174
- Josey S, Kent E, Taylor P (1999) New insights into the ocean heat budget closure problem from analysis of the SOC air-sea flux climatology. *J Clim* 12:2856–2880
- Kiehl JT, Gent PG (2004) The community climate system model, version 2. *J Clim* 17:3666–3682
- Kim S-J, Stössel A (2001) Impact of subgrid-scale convection on global thermohaline properties and circulation. *J Phys Oceanogr* 31:656–674
- Kraus EB, Turner JS (1967) A one-dimensional model of the seasonal thermocline II. The general theory and its consequences. *Tellus* 19:98–105
- Large W, McWilliams J, Doney S (1994) Oceanic vertical mixing: a review and a model with a nonlocal boundary layer parameterization. *Rev Geophys* 32:336–403
- Levitus S, Burgett R, Boyer TP (1994) NOAA World Ocean Atlas 1994, vol 3 and 4. Natl Oceanogr Data Cen, Washington, DC, pp 99, 117
- McDougall TJ, Dewar WK (1998) Vertical mixing and cabbeling in layered models. *J Phys Oceanogr* 28:1458–1480
- Meehl GA, Arblaster JM, Strand WG Jr (2000) Sea-ice effects on climate model sensitivity and low frequency variability. *Clim Dyn* 16:257–271
- Meehl GA, Gent PR, Arblaster JM, Otto-Bliesner BL, Brady EC, Craig A (2001) Factors that affect the amplitude of El Niño in global coupled climate models. *Clim Dyn* 17:515–526
- Olbers D, Borowski D, Völker C, Wolff J-O (2004) The dynamical balance, transport and circulation of the Antarctic Circumpolar Current. *Antarct Sci* 16(4):439–470
- Orsi AH, Whitworth T III (2004) Hydrographic Atlas of the World Ocean circulation experiment (WOCE), vol 1: Southern Ocean. In: Sparrow M, Chapman P, Gould J (eds) International WOCE Project Office, Southampton, U.K., ISBN 0-904175-49-9
- Paluszkiwicz T, Romea RD (1997) A one-dimensional model for the parameterization of deep convection in the ocean. *Dyn Atmospheres Oceans* 26:95–130
- Pope VD, Stratton RA (2002) The processes governing resolution sensitivity in a climate model. *Clim Dyn* 19:211–236
- Prather MJ (1986) Numerical advection by conservation of second-order moments. *J Geophys Res* 91:6671–6680
- Roberts MJ, Banks H, Gedney N, Gregory J, Hill R, Mullerworth S, Pardaens A, Rickard G, Thorpe R, Wood R (2004) Impact of an eddy-permitting ocean resolution on control and climate change simulations with a global coupled GCM. *J Clim* 17:3–20
- Romanou A, Rossow WB, Chou SH (2005) Decorrelation scales of high resolution turbulent fluxes at the ocean-surface and a method to fill in gaps in satellite data products. *J Clim* (in press)
- Russell GL, Lerner JA (1981) A new finite-differencing scheme for the tracer transport equation. *J Appl Meteorol* 20:1483–1498
- Russell GL, Miller JR, Rind D, Ruedy R, Schmidt G, Sheth S (2000) Comparison of model and observed regional temperature changes during the past 40 years. *J Geophys Res* 105:14891–14898
- Schmidt GA et al (2005) Present day atmospheric simulations using GISS ModelE: comparison to in-situ, satellite and reanalysis data. *J Clim* (in press)
- Schmitz WJ Jr (1995) On the interbasin-scale thermohaline circulation. *Rev Geophys* 33:151–173
- Smagorinsky J (1963) General circulation experiments with the primitive equations. *Mon Wea Rev* 91:99–164
- Sokolov AP, Forest CE, Stone PH (2003) Comparing oceanic heat uptake in AOGCM transient climate change experiments. *J Clim* 16:1573–1582
- Speer K, Guilyardi E, Madec G (2000a) Southern ocean transformation in a coupled model with and without eddy mass fluxes. *Tellus* 52A:554–565
- Speer K, Rintoul R, Sloyan BM (2000b) The diabatic Deacon cell. *J Phys Oceanogr* 30:3212–3222
- Steele M, Morley R, Ermold W (2001) PHC: a global ocean hydrography with a high-quality Arctic Ocean. *J Clim* 14:2079–2087

- Stommel H, Arons AB (1960) On the abyssal circulation of the world ocean I: stationary planetary flows patterns on a sphere. *Deep Sea Res* 6:140–154
- Stössel A, Yang K, Kim SJ (2002) On the role of sea ice and convection in a global ocean model. *J Phys Oceanogr* 32:1194–1208
- Stratton RA (1999) A high resolution AMIP integration using the Hadley Centre model HadAM2b. *Clim Dyn* 15:9–28
- Sun S, Bleck R (2001a) Atlantic thermohaline circulation and its response to increasing CO<sub>2</sub> in a coupled atmosphere–ocean model. *Geophys Res Lett* 28:4223–4226
- Sun S, Bleck R (2001b) Thermohaline circulation studies with an isopycnal coordinate ocean model. *J Phys Oceanogr* 31:2761–2782
- Sun S, Hansen J (2003) Climate simulations for 1951–2050 with a coupled atmosphere–ocean model. *J Clim* 16:2807–2826
- Talley L, Reid JL, Robbins PE (2003) Data-based meridional overturning streamfunctions for the global ocean. *J Clim* 16:3213–3226
- Trenberth KE, Caron JM (2001) Estimates of meridional atmosphere and ocean heat transport. *J Clim* 14:3433–3443
- Wadley MR, Bigg GR (1996) Abyssal channel flow in ocean general circulation models with application to the Vema Channel. *J Phys Oceanogr* 26:38–48
- Whitworth T, Peterson RG (1985) Volume transport of the Antarctic Circumpolar Current from bottom pressure measurement. *J Phys Oceanogr* 15:810–816
- Wood RA, Keen AB, Mitchell JFB, Gregory JM (1999) Changing spatial structure of the thermohaline circulation in response to atmospheric CO<sub>2</sub> forcing in a climate model. *Nature* 399:572–575
- Zhang J, Rothrock D (2000) Modeling Arctic sea ice with an efficient plastic solution. *J Geophys Res* 105:3325–3338
- Zhang Y-C, Rossow WB, Lacis AA, Oinas V, Mishchenko MI (2004) Calculation of radiative fluxes from the surface to top of atmosphere based on ISCCP and other global datasets: refinements of the radiative transfer model and the input data. *J Geophys Res* 109:D19105. DOI 10.1029/2003JD004457